August 2020

Nuclear Magnetic Resonance Under Extreme Conditions

Anand Prashant Dwivedi
University of Wisconsin-Milwaukee

NUCLEAR MAGNETIC RESONANCE UNDER EXTREME CONDITIONS

by

Anand Prashant Dwivedi

A Thesis Submitted in

Partial Fulfillment of the

Requirements for the Degree of

Master of Science

in Physics

at

The University of Wisconsin-Milwaukee

August 2020

ABSTRACT

NUCLEAR MAGNETIC RESONANCE UNDER EXTREME CONDITIONS

by

Anand Prashant Dwivedi

The University of Wisconsin-Milwaukee, 2020
Under the Supervision of Professor Prasenjit Guptasarma

Nuclear Magnetic Resonance (NMR) is a prime characterization tool used to understand the structures and interactions in organic molecules, crystals, as well as non-crystalline materials. However, until now, the combination of NMR with high-pressure instrumentation such as Diamond Anvil Cells (DAC) was deemed unfeasible due to the high spatial and electrical costs of standard NMR electromagnets or the regular refill of cryogenic liquids for superconducting magnets. Standard NMR techniques also raises technical difficulties when combining high-pressure instrumentation with high-temperature techniques such as laser heating. In the first part of this thesis, we present the development of a low-cost and space-saving table-top NMR system based on Halbach magnet arrays. We also demonstrate the use of this setup with a double-sided laser heating system for simultaneous *in situ* high-pressure and high-temperature studies. The feasibility of this setup is demonstrated by collecting ^{1}H-NMR spectra of water at 25 GPa and 1063 (50) K. This introduced setup is shown to yield ^{1}H-NMR signals of similar spectral resolution in DAC-based experiments as standard electromagnets operating around the same magnetic fields. In the second part of this thesis, we report low-temperature NMR measurements, that, along with other measurement techniques, reveal Charge Density Wave (CDW) order in the topological insulator Bi_2Se_3.

TABLE OF CONTENTS

LIST OF FIGURES

LIST OF TABLES

Chapter 1

Introduction

In this thesis, we present Nuclear Mangetic Resonance (NMR) studies carried out under extreme conditions. High-pressure and high-temperature NMR was conducted at the Bayerisches Geo-institute, University of Bayreuth, Germany, in the lab of Dr. Leonid Dubrovinsky, in collaboration with Thomas Meier, Timofey Fedotenko, Saiana Khandarkhaeva and Natalia Dubrovinskaia. Low-temperature high magnetic-field NMR was conducted at the National High Magnetic Field Laboratory in the lab of Dr. Arneil Reyes in collaboration with Yanan Li and Christian Parsons of Dr. Prasenjit Guptasarma's lab at the University of Wisconsin-Milwaukee.

Chapter 1 briefly describes the instrumentation used to achieve high pressures, Diamond Anvil Cells (section 1.1), the principles of Nuclear Magnetic Resonance (section 1.2), Halbach array magnets, which are shown to be a low-cost replacement to the standard NMR electromagnets (section 1.3), and the breakthrough technique of Lenz lenses (section 1.4) that allowed for the application of NMR to the tiny sample spaces in Diamond Anvil Cells. Sections 1.5 and 1.6 describe the background for low-temperature high-magnetic field NMR with section 1.5 describing the unique class of materials called topological insulators which behave as insulators in their bulk but have conducting edge or surface states. Section 1.6 discusses the concept of Charge Density Waves that have been revealed using NMR techniques

along with other resistivity measurements and electron diffraction.

Chapter 2, section 2.1 describes the experimental setup used to carry out the high-pressure high-temperature NMR studies and section 2.2 describes the low-temperature instrumentation.

Chapter 3 presents the results of high-pressure high-temperature NMR studies and Chapter 4 presents the results of low-temperature high magnetic-field NMR.

High pressure research in materials science and geosciences has led to the discovery of some fascinating and unexpected phenomena. For example, under extremely high pressures of 1 to 2 GPa, water and methane start to mix together [1]. Pruteanu et al suggest that the two compounds could mix well because the methane molecules got compressed to the point where they could slip into the network of bonds connecting all the water molecules and distribute themselves evenly [1]. Methane and water also occur on other planets in our solar system where the pressure can be really high. Studying how these molecules react under extreme conditions can open doors to reveal the chemistry taking place in places that are often impossible to visit. As another example, chemically inert helium which is not known to form thermodynamically stable compounds, combines with sodium to form thermodynamically stable sodium helide Na_2He under a pressure of 113 GPa [2]. High pressures also have an interesting effect on the conductive properties of materials. Under high pressures, non-metals, most of which are insulators, start behaving like conducting metals. The reverse is also true where high pressure alters the overall structure of the metal by locking the electrons between atoms and hence displaying a non-metal like phenomena.

High pressures also lead to myriad novel physical phenomena such as the symmetrisation of hydrogen bonds in ice VII at 75 GPa which are governed by quantum-mechanical tunneling of protons within the hydrogen bond network [3] or the observation of the formation of a free electron hydrogen sublattice in metal hydrides above 100 GPa [4]. In recent years, metal hydrides have been found to be one of the prime candidates for high temperature

superconductivity. In a theoretical work, researchers have developed a theory that suggests a ternanry hydride Li_2MgH_{16} should become superconducting at a temperature of approximately 473 K and pressure of 250 GPa [5]. High pressure and high temperature studies hold the key to the search for room-temperature superconductivity which could be a major solution to our energy problems.

Different experimental techniques can be used to study matter when it is subjected to high pressures. Among these many techniques, Nuclear Magnetic Resonance or NMR is a powerful tool to study the physical and chemical properties of matter. NMR was first reported in 1945 by two groups of physicists: group led by Edward Purcell at Harvard University that reported the detection of NMR signals in solid paraffin, and the group led by Felix Bloch at Stanford University that found the signals in liquid water. Purcell and Bloch shared the 1952 Nobel Prize in Physics "for their development of new methods for nuclear magnetic precision measurements and discoveries in connections therewith". Ever since its first discovery, enhancements were made to the techniques of NMR and it now has been established as one of the prime characterization techniques to understand the structures and interactions in organic molecules, crystals as well as non-crystalline materials. One of the prime applications of NMR was realized by chemist Paul Lauterbur who shared the 2003 Nobel Prize in Physiology or Medicine "for their discoveries concerning magnetic resonance imaging" or MRI.

1.1 Diamond Anvil Cell

Percy Bridgman is known as the creator of the field of high-pressure experimentation [6], for which he received the 1946 Nobel Prize in Physics. The Diamond Anvil Cell (DAC), which was an outgrowth of Bridgman's simple squeezer, was invented in 1958 almost simultaneously by researchers at the National Bureau of Standards (now National Institute of Standards and Technology) and at the University of Chicago. DAC revolutionized the field of high pressure

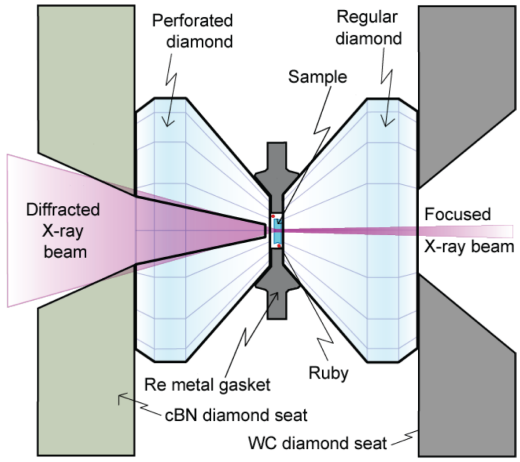

Figure 1.1: A generalized diamond anvil cell assembly with labeled components. Adapted from [8]

research because for the first time a handheld device could create pressures comparable to the pressure inside the core of Earth and other planets. Some enhancements to the DAC have now been shown to produce pressures of over 1 Terapascal [7]. One of the major advantages that DACs had over its predecessors was that diamonds are transparent to a wide range of electromagnetic wavelengths including gamma rays, X-rays, visible light and much of the infrared and ultraviolet region. DACs, for the first time, thus provided researchers the chance to visually observe the effects of pressure and also access to different kinds of experimental techniques such as X-ray diffraction and Raman spectroscopy. Another advantage is the static pressure that DAC provides to the sample.

The components of a DAC are shown in Figure 1.1 and briefly explained below.

- **Diamond Anvil**

Typically, the diamonds are 0.5 - 1 carat in size (1 carat = 200 mg). Unlike regular diamonds used in jewelry where the edges of the diamond converge at a single point, the edges of the DAC meet at a flat surface called the culet whose diameter is in the range of 100 - 250 μm.

- **Sample**

Since diamonds are inert, different kinds of samples including solids and liquids can be examined using a DAC. In the simplest scenario, a powder of a solid is placed between the diamond heads. When the diamonds are pushed together, the sample takes the form of a circular film, where the center of the film is at maximum pressure while the edges are still at atmospheric pressure, thus leading to a large pressure gradient across the sample. This method of directly loading the sample between the diamond heads does not work for liquids or for samples that cannot support shear stress. To alleviate the stress in the sample, the sample is placed in a gasket which is described next. Typically, the volume of the sample in a DAC is around 40 pl.

It is extremely important that the two diamond heads are aligned perfectly before pushing on the sample, as a slight misalignment can cause the diamonds to slip on each other causing fracture and hence destroying both the diamonds.

• **Gasket**

A gasket is a thin metal foil that has a small hole in its center which is used to contain the sample. The hole is typically used for liquid samples. The pressure gradient is distributed over the gasket and hence spares the sample of the large pressure gradient. Strong and stiff metals such as rhenium or tungsten are commonly used for making gaskets. For experiments where X-rays need to pass through the sample, the gaskets made up of boron [9], boron nitride [10] or diamond [11] are used since rhenium and tungsten are not transparent to X-rays.

• **Diamond Seats**

The diamonds sit in "seats" that connect them to the rest of the structure of the cell. Once diamonds are placed in the seats, the position of the seats is adjusted to align the diamonds. The seats are made up of strong materials since they transmit the force from the cell to the diamond.

• **Ruby**

One of the ways to measure the pressure inside the sample chamber is to measure the unit cell size of a material whose equation of state is well known. However, one of the more common and accurate ways is to measure the position of the fluorescence lines of Ruby placed within the sample chamber, the positions of which are known as a function of pressure. Ruby is chemically inert and has a strong fluorescence when irradiated by a green laser light. This method of measuring pressure does not usually work when the DAC setup is coupled with an external heating system such as resistance heating or laser heating because the fluorescence peaks of Ruby broaden and decrease in intensity at high temperatures.

1.2 Nuclear Magnetic Resonance

Only the nuclei that possess a spin can be probed using NMR. The magnetic dipole moment of a proton is given by $\vec{\mu_p} = 2.7928\ \mu_B$ where μ_B is the Bohr magneton. When any magnetic dipole moment is placed inside an external magnetic field, that magnetic field exerts a torque on the dipole moment that tends to orient the dipole moment along the external magnetic field. The magnetic dipole moment does not align perfectly with the external magnetic field, but instead precesses around an axis with frequency known as the Larmor frequency which is given by

$$\omega_0 = \gamma B_0 \tag{1.1}$$

where γ is the gyromagnetic ratio of the nucleus and B_0 is the strength of the external magnetic field. When the external magnetic field is applied, the NMR-active nuclei gets distributed into different energy levels defined by the orientation of their magnetic moments with respect to the external magnetic field. This effect on their alignment is demonstrated in Figure 1.2 for a nucleus with spin quantum number equal to 1/2. The spin states that align themselves along the direction of the external magnetic field are at lower energy than the spin states that are aligned against the direction of the external magnetic field. The energy separation ΔE between these states is relatively small, and the energy from thermal

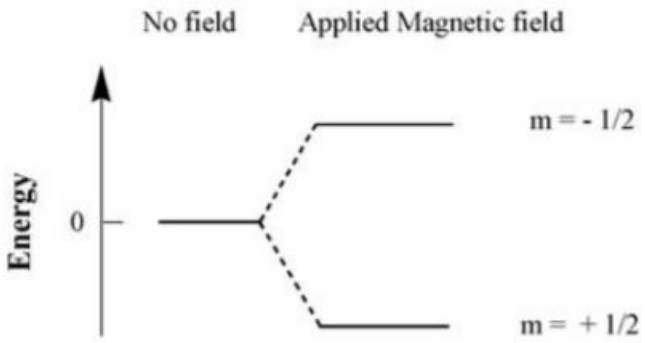

Figure 1.2: Energy levels for a nucleus with spin quantum number 1/2. Adapted from [1]

collisions is sufficient enough to place many nuclei into the higher energy spin state. This energy separation is given by the equation

$$\Delta E = hB_0\gamma \tag{1.2}$$

where h is the Planck's constant. The Boltzmann distribution describes the number of nuclei in each spin state.

$$\frac{N_+}{N_-} = e^{-\frac{\Delta E}{kT}} \tag{1.3}$$

where N_+ and N_- represent the number of nuclei in the higher and lower energy spin states respectively. The energy difference between these energy states is bridgeable by photons in the radio-frequency (RF) region of the electromagnetic spectrum with

$$\Delta E = hf \tag{1.4}$$

where f is the frequency of the photon. When the nuclei are irradiated with this RF pulse, promotion among the spin states occur when the frequency of the RF pulse matches the energy difference shown in Figure 1.2. This is the resonance condition. The excited nuclei give back their excess energy and return to lower spin states (spin flipping). This relaxation process can occur via two pathways: either by interaction with the environment (lattice) or by exchanging energy with neighbouring nuclei at lower energy levels [12]. The former

process is called spin-lattice relaxation and is characterized by a time constant T_1 called the spin-lattice relaxation time, while the latter process is described by a time constant T_2 called the spin-spin relaxation time. When the nuclei transition between energy states, their frequency also changes. This change in frequency is measured as a "chemical shift". Different atoms have different chemical shifts and by determining these chemical shifts along with other parameters, the composition and interactions within the sample molecule can be found.

1.3 Halbach magnet array

Invented by physicist Klaus Halbach at Lawrence Livermore National Laboratory, Halbach arrays use an arrangement of permanently magnetized rare earth magnets. The magnetization axis of each magnet in the array is oriented such that the array creates a strong and homogeneous field at the center of the magnet. One of the common rare earth magnets used in the Halbach array is an alloy of neodymium. Figure 1.3(a) shows a Halbach array magnet that is made up of eight separate permanent magnets with different axes of magnetization. The Diamond Anvil Cell is placed in the cavity at the center of the array. Figure 1.3(b) shows a Finite Element Method Magnetics (FEMM) simulation of the Halbach array in Figure 1.3(a) indicating the density plot of the magnetic field intensity. Pink color indicates the strongest magnetic field. It is clear from Figure 1.3(b) that the magnetic field is homogeneous and strongest at the central cavity of the magnet.

Similar to ferromagnetic materials such as iron, rare-earth elements can be magnetized to become permanent magnets, but the Curie temperature (temperature above which ferromagnetism is lost) of rare-earth metals is below room temperature. However, when rare-earth elements forms compounds with transition metals such as iron, nickel or cobalt, their Curie temperature rises well above room temperature. Therefore, rare-earth magnets used in a Halbach array are an alloy of rare-earth and transition metals. The high magnetic field

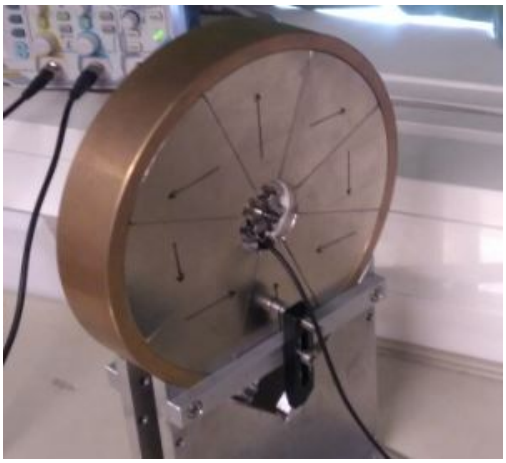

(a) Black arrows indicate the magnetization axis of each individual magnet

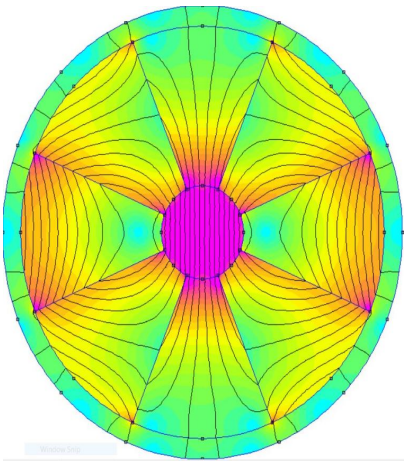

(b) FEMM simulation of the Halbach array in Figure 1.3(a) indicating the density plot of the magnetic field strength

Figure 1.3: Halbach array magnet

strength of rare-earth magnets arises from the high magnetic anisotropy of their crystalline structure. Also, the atoms of rare-earth metals tend to have high magnetic moments resulting from unpaired electrons in their orbital structure, and an incomplete filling of the f-shell that can contain up to seven unpaired electrons.

1.4 High-pressure NMR

Combining high-pressure research in Diamond Anvil Cells (DAC) with a probing technique like Nuclear Magnetic Resonance (NMR) opens up the exciting field of high-pressure NMR. However, as noted in Section 1.1, the sample space in the DAC is extremely small, and one of the major obstacle is the difficulty in focusing the magnetic field required for NMR in the small sample space for DACs. Recently, researchers made enhancements to magnetic lenses, know as a "Lenz lens" that enabled the high precision application of NMR in tiny spaces [13, 14]. The Lenz lens acts like a flux transformer with its outer winding collecting flux from a larger area and the inner anti-winding depositing this flux over the very small sample area. Very soon after this work, researchers were able to apply the concept of Lenz

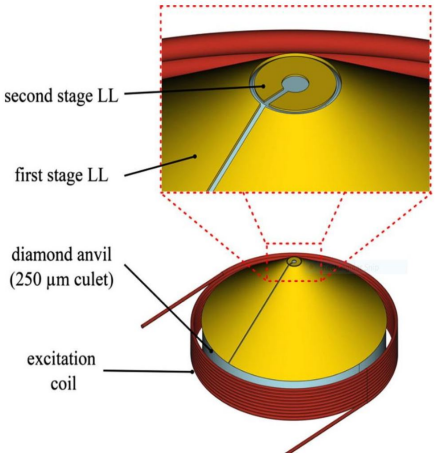

(a) Lenz lens on the diamond. Adapted from [16]

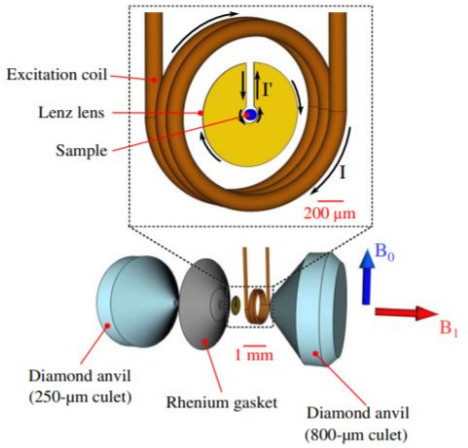

(b) Using Lenz lens combined with NMR. Adapted from [15]

.

Figure 1.4: Lenz lens in Diamond Anvil Cell

lens in a DAC [15] which accelerated the field of high-pressure NMR. Figure 1.4(a) shows the Lenz lens on a diamond in the DAC.

Figure 1.4(b) demonstrates the use of Lenz lens with NMR where the blue and red arrows denote the direction of the external magnetic field and the direction of the radio-frequency field, respectively, generated by the excitation coil and the lens.

Most high pressure NMR experiments in DACs so far have been performed at either cryogenic or ambient temperatures. One of the prime reasons that the application of this method at higher temperatures was considered unlikely is the spatial and cost requirements for NMR equipment such as superconducting magnets that prohibit a combination with external electrical heating or with sensitive optical equipment necessary for *in situ* laser heating in DACs.

The first part of this thesis focuses on the development of a low-cost and space-saving table-top NMR setup using a Halbach array magnet design usable for diamond anvil cells. Furthermore, this setup demonstrates the combination of high-pressure and high-temperature *in situ* NMR measurements [17].

1.5 Topological Insulator

In the past decade, a new class of materials called topological insulators have caught the attention of the condensed matter community. The 2016 Nobel Prize in Physics was awarded to David Thouless, Duncan Haldane and Michael Kosterlitz "for theoretical discoveries of topological phase transitions and topological phases of matter". However, one of the earliest studies on this class of materials was conducted in 2005 by Charles Kane and Eugene Mele at the University of Pennsylvania, where they reported the conversion of graphene from an ideal two-dimensional semi-metallic state to a quantum spin Hall insulator [18].Interestingly, this electronic state of matter is gapped in the bulk but supports spin and charge transport in the gapless edge states.

The quantum Hall effect (1985 Nobel Prize in Physics) is a phenomenon having topological features that can be observed in certain materials when a large magnetic field is applied. As can be visualized from Figure 1.5, the electrons in the bulk get confined to small orbits under the influence of a magnetic field, hence making the material insulating in the bulk. However, along the edges, the electrons only have partially complete trajectories and hence keep moving giving rise to the conducting "edge states". Recently, Quantum Spin Hall (QSH) [19] states have been observed in certain materials. QSH systems have an energy gap separating the valence and conduction bands in their bulk, leading to an insulating bulk state, but on the boundary they have gapless edge or surface states that are topologically protected and immune to geometric perturbations [18, 20, 21]. Unlike Quantum Hall states that require an external magnetic field which breaks time-reversal (TR) symmetry, QSH states are TR invariant and do not require an applied field.

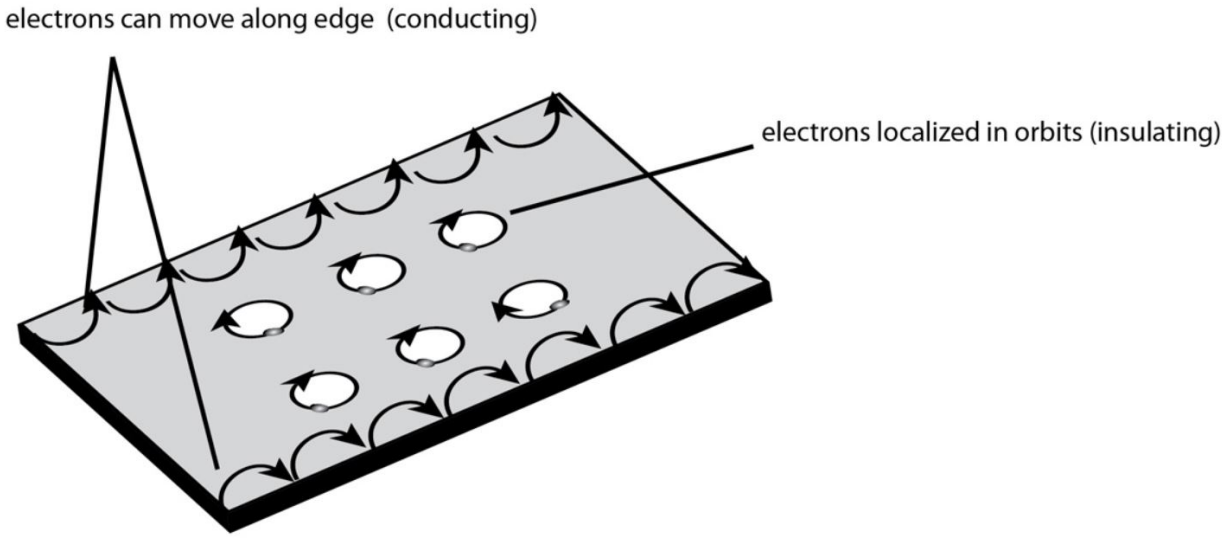

Figure 1.5: Quantum Hall effect. Under an externally applied magnetic field, the electrons in the bulk are confined to tiny orbits giving the material insulating properties in the bulk, while the incomplete trajectories on the edges gives rise to conducting "edge states". Adapted from [22]

.

1.6 Charge Density Waves

A charge density wave (CDW) is an example of a cooperative state in which the ionic lattice and electron gas both develop a distortion to lower the total free energy of the sample [23]. It is a static modulation of conduction electrons and is a Fermi-surface driven phenomenon which is usually accompanied by a periodic lattice distortion, as first suggested by Rudolf Peierls in 1955 and as shown in Figure 1.6. The first Brillouin zone (primitive cell of the reciprocal lattice) with boundary at $\pm\pi/a$ is half occupied. The electronic charge density is of the periodic form, being maximum in the vicinity of the ion cores. The figure on the right in Figure 1.6 shows the periodic distortion of the one-dimensional lattice, causing the formation of a charge density wave of period $2a$ associated with the new superlattice. Since the lattice has been doubled in real space, a new band gap appears at $\pm\pi/2a$ in k-space which lowers the Fermi energy. A structural change occurs when the CDW formation is accompanied by

ion displacements that stabilize the charge perturbation. Another requirement for forming a CDW is a strong electron-phonon coupling, required to permit ionic displacements to reduce the otherwise prohibitive Coulomb energy [24].

Studying charge density waves is interesting because it is intimately linked to superconductivity [25–29], which is believed to also arise from electron-lattice interactions. In some cases, superconductivity competes with CDW for the same conduction electrons to form Cooper pairs, while in other cases CDW assists superconductivity through its coupling to crystal lattice vibrations (phonons) that act as a "glue" between electrons forming the Cooper pair.

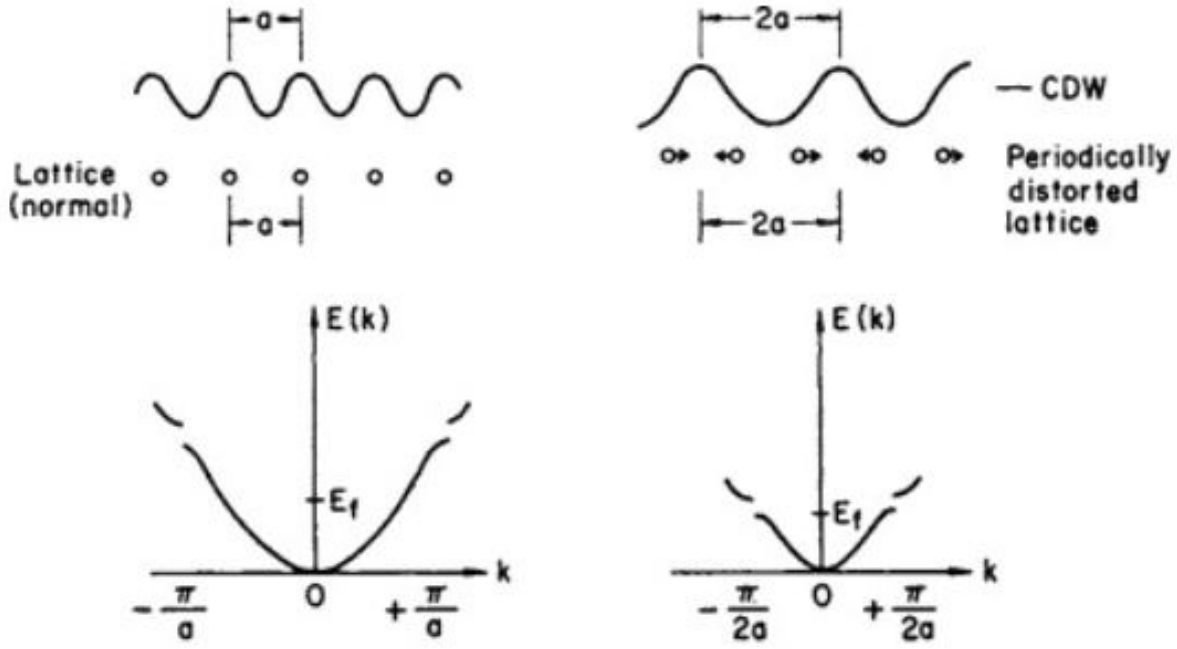

Figure 1.6: Schematic diagram showing a periodic lattice distortion, charge density waves, and energy band gaps before and after a periodic lattice distortion in a hypothetical one-dimensional metal. Note the overall lowering of the Fermi level following the periodic lattice distortion. Adapted from [24]

.

Chapter 2

Experimental Methods

2.1 High-pressure high-temperature NMR

2.1.1 Diamond Anvil Cell preparation

Two BX90 [30] type Diamond Anvil Cells were prepared with cell no. 1 using 250μm diamonds and cell no. 2 using 100 μm diamonds. BX90 type cells are highly stable and use a 90-degree symmetrical axial opening making it suitable to be used with a wide range of experiments such as single-crystal X-ray diffraction and resistivity measurements and also with double-sided laser heating. A description of the parts of a BX90 DAC is illustrated in Figure 2.1.

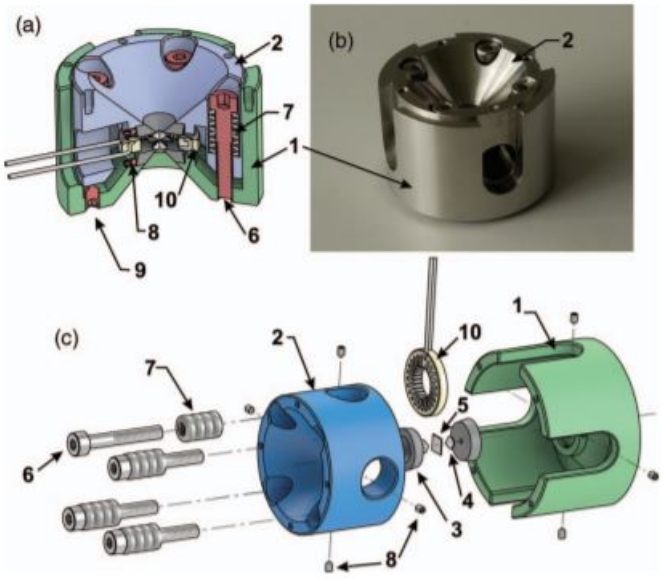

Figure 2.1: BX90 diamond anvil cell design. (a) Section view, (b) photograph of a loaded cell, (c) exploded view. (1) Outer cylinder part, (2) inner piston part, (3) diamond supporting plates, (4) diamond anvils, (5) metallic gasket, (6) M4 (8-32) screws for generating loading force, (7) pack of conical spring washers (Belleville springs), (8) setscrews for diamond anvils alignment, (9) safety setscrews, (10) optional miniature resistive heater. Adapted from [18]

Using a different mount setup, the diamond anvils were placed in the seats (described in section 1.1) and glued to the seat cavity using epoxy glue. Figure 2.2 shows the seat preparation procedure. This mount setup with the seat and diamond anvil was then placed on the hot plate (75°C) for 30 minutes to allow for the glue to harden. The seat was then taken out from the mount setup and placed in the BX90 DAC as shown in Figure 2.3.

A similar process was done for the other half of the cell. Once both the anvils were placed in their respective halves of the cell, the diamond anvils (and the seats) were aligned within the cell by bringing the diamonds very close to each other (within a few micrometers) and adjusting the set screws holding the seats in place from all four sides. A safety screw was placed from one end of the cell. The lead screw was tightened while the safety screw retracted in order to make sure that the diamond heads don't come in contact. It is important that the diamond anvils are aligned perfectly before they are pressed against each other on the sample, because even a slight misalignment can cause the anvils to slip and damage them.

(a) Centering and aligning the seat to place the diamond anvils. Note this is not the DAC.

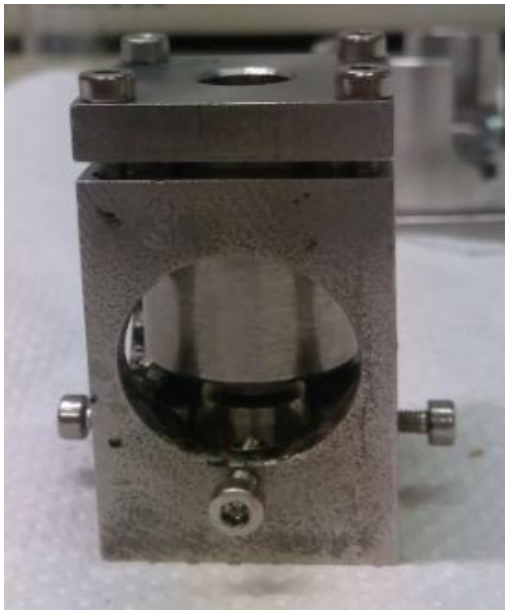

(b) Once diamond anvils are glued to the seats, the top mount is closed allowing for the diamond anvils to set in the seats firmly.

Figure 2.2: Diamond Anvil Cell seat preparation

The anvils were then cleaned using ethanol and compressed air to remove the excess glue from the surface that might give spurious signals during NMR measurements. The rhenium gasket was then placed in between the diamond heads and the DAC was closed. The pressure was callibrated using the shift of the first order Raman spectrum of the diamond edge at the center of the anvil's culets. Both cells were pressurized to about 25 GPa. The cell was then opened back up to remove the gasket. The thickness of the gasket for cell no. 1 was 36 μm and that for cell no. 2 was 28 μm. Then a hole was cut in the center of the gasket using a laser beam. This hole contained the sample.

Next, the Lenz lens resonators (as described in section 1.4) were prepared by covering each diamond with a 1 μm thick layer of copper using physical vapor deposition. The part of the backing plate other than the anvils was covered with copper tape to avoid depositing copper anywhere else than the anvils. The lens structure was then cut on top of this layer using focused ion beam milling. For electrical insulation, the gasket placed between the

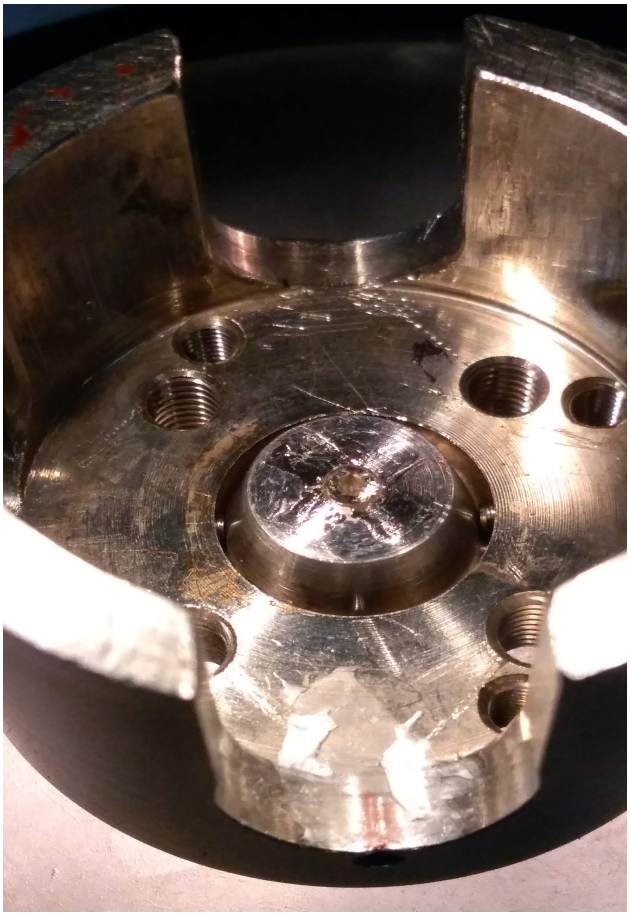

Figure 2.3: Prepared seat and diamond anvil placed in the lower half of the BX90 pressure cell.

diamond heads (as described in section 1.1) was covered with 500 nm thick layer of Al_2O_3 using chemical vapor deposition. The excitation coils (as labeled in Figure 1.4) were made with a 80 μm thick PTFE insulated copper wire, consisting of 4 turns and 3 mm coil diameter. Varnish was used to hold the turns of the coil together. These coils were glued to the backing plate with the diamond anvil at its center as shown in Figure 2.4.

Both cells were loaded with distilled water, which was the sample, and with gold powder which acted as absorber targets during near infrared laser heating. Both cells were then dried to avoid spurious ^{1}H-NMR signals from outside the sample chamber within the DAC.

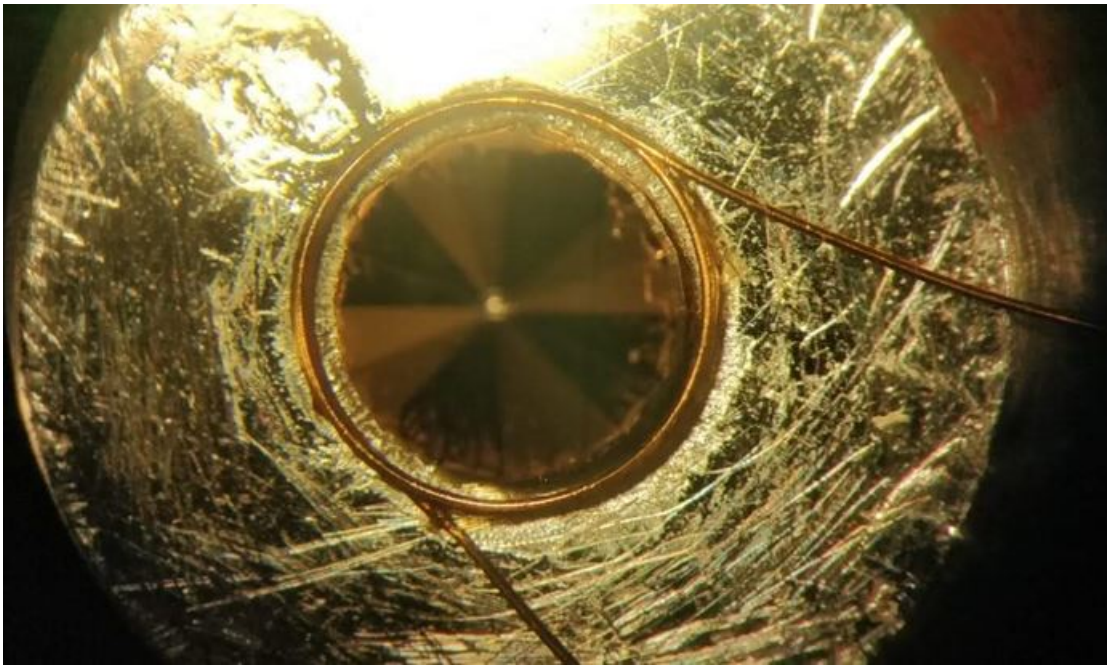

Figure 2.4: Excitation coil glued to the seat with diamond anvil at its center.

2.1.2 NMR Measurements

The magnetic field required for the NMR experiments was generated by a Halbach array magnet as described in section 1.3. The field produced at the center of the magnet was about 1 T. The magnet has a diameter of 250 mm, height of 40 mm, and a central circular hole of 45 mm diameter. The Diamond Anvil Cell sits in this central hole. Spin echo excitation [31] (described below) was used for signal acquisition.

In 1946, Felix Bloch and Edward Purcell (mentioned in section 1.2) used a continuous wave technique that used a fixed radio-frequency (RF) field B_1 while the main magnetic field B_0 was swept through resonance. Around the same time, Erwin Hahn implemented a pulsed technique where B_0 is held constant while the B_1 field at the Larmor frequency is pulsed on and off. Hahn observed a transient oscillation in the signal, which today is more commonly referred to as Free Induction Decay (FID). The FID is a damped signal of the form as shown in Figure 2.5 and described by the equation

$$[sin\omega_0 t]e^{\frac{-t}{T_2^*}} \tag{2.1}$$

where the signal is damped by a process called T_2^*-decay. T_2^* is usually much smaller than the spin-spin relaxation time T_2 and they are related by Equation 2.2.

$$\frac{1}{T_2^*} = \frac{1}{T_2} + \gamma \Delta B_0 \tag{2.2}$$

where γ is the gyromagentic ratio and ΔB_0 is the difference in strength of the locally varying field [32].

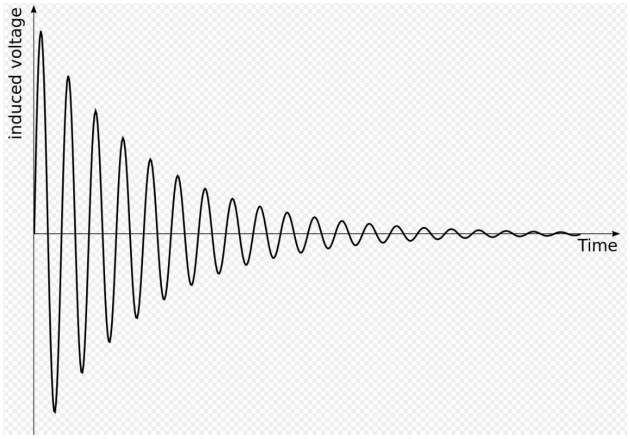

Figure 2.5: FID signal damped by T_2^*-decay. Adapted from [33]

T_2 is the time constant for the decay of transverse magnetization arising from natural interactions at the atomic or molecular level. However, in a real NMR experiment, the transverse magnetization decays much faster than predicted by the natural atomic or molecular mechanisms. This "real" rate of decay is characterized by the time constant T_2^* [34]. A single RF pulse generates a FID, but two successive RF pulses produce a spin echo. The time between the middle of the first RF pulse and the peak of the spin echo is called the echo time (TE) as shown in figure 2.6.

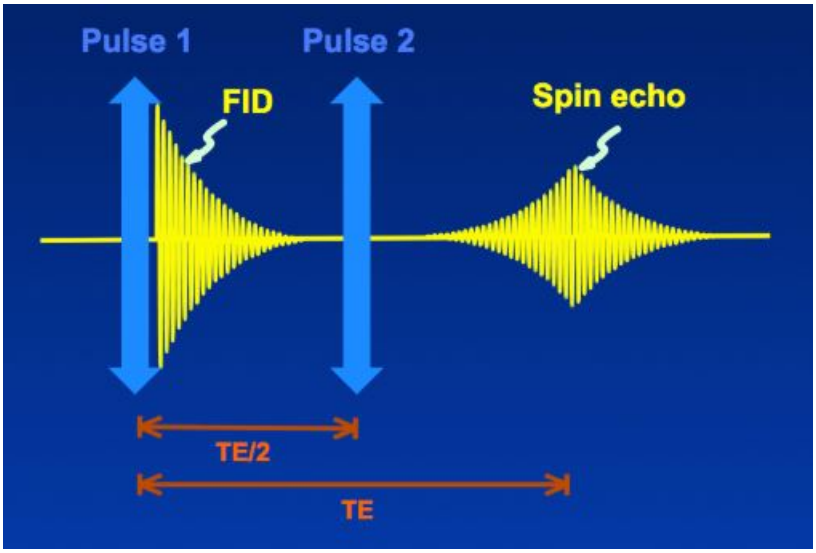

Figure 2.6: The first RF pulse generates the FID, while the second pulse generates the spin echo. TE represents the echo time. Adapted from [35]

Spin echo has been used in other experiments on ice VII [3]. In this experiment, a 300 ns long acquisition delay was used due to the broad ^{1}H-NMR spectra of ice VII, which is the cubic crystalline form of ice. Figure 2.7 shows the phase diagram of water. All recorded spectra were found to be free of base line distortions, which are characteristic at such short pulse dead times using standard NMR equipment. Using nutation experiments, which is the periodic variation in the inclination of the rf pulse, $\pi/2$ pulses of 3 μs for cell no. 1 and 1 μs for cell no. 2 were used at average pulse power of about 20 W. Figure 2.8 shows the nutation profiles. For both cells, the spin lattice relaxation times were about 70 ms. Relaxation delays are chosen to allow for full relaxation of the excited spin systems.

To callibrate the magnetic field along the z-axis of the Halbach array magnet (perpendicular to the magnet's main plane), the position of cell no. 1 was changed in steps of 0.5 mm. Figure 2.9 shows the simulation of the magnetic field in the x-y place of the magnet. The resulting center of gravity in frequency space was used an an internal primer of the polarizing external magnetic field B_0 in the sample chamber using the relationship

$$\omega_0 = \gamma_n B_0 \tag{2.3}$$

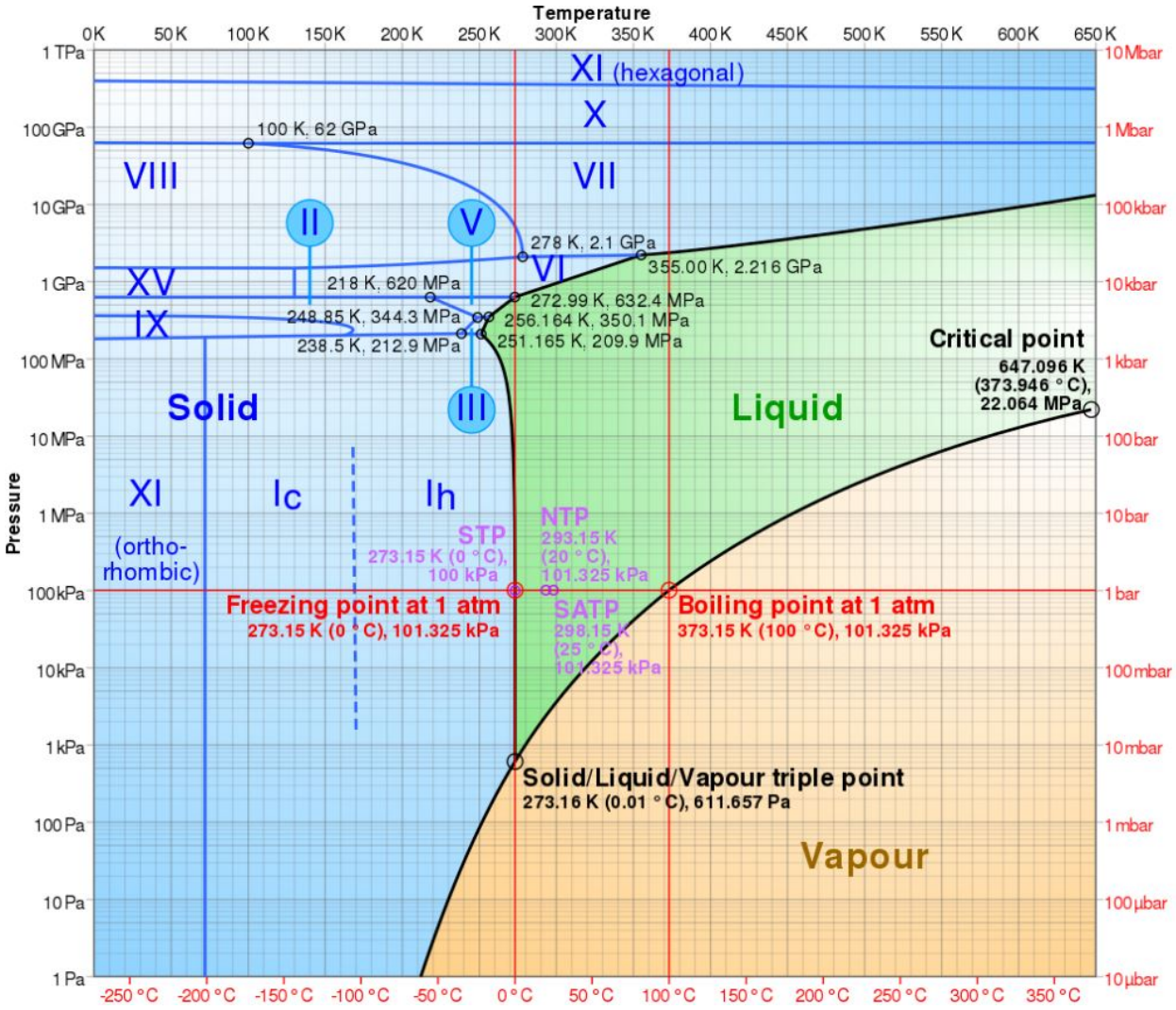

Figure 2.7: Phase diagram of water. Adapted from [36]

2.1.3 Laser Heating

The double-sided laser heating setup developed in Reference [37] was used for the high-temperature experiments. Configuration of the laser heating setup is demonstrated in Figure 2.10. This transferable setup has been demonstrated to be combined with synchrotron beamline equipment by performing *in situ* X-ray Transmission Microscopy imaging at the ID15B beamline of the European Synchrotron Radiation Facility [37]. Its flexible design allows simple interchange of laser sources and focusing optics for applications in different types of experiments. This setup is designed to improve the accuracy of temperature mea-

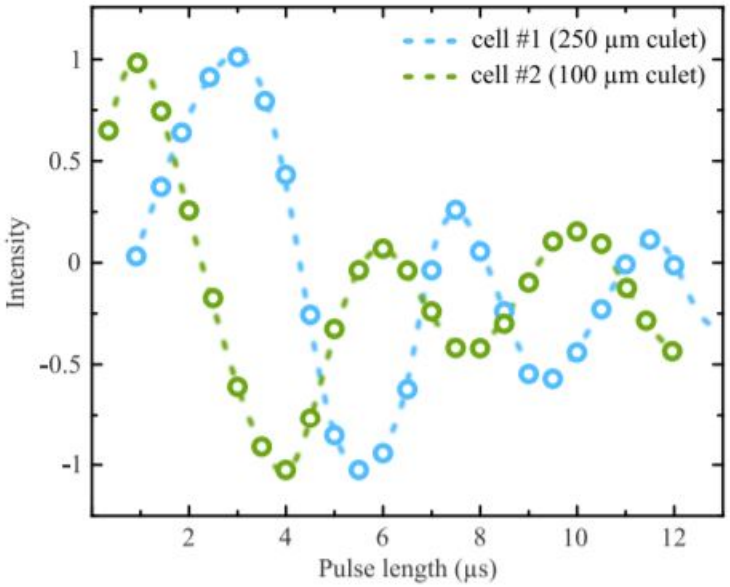

Figure 2.8: Nutation profile of the two DAC cells at 20 W pulse power. Pulses were incremented in steps of 500 ns up to 10 μs.

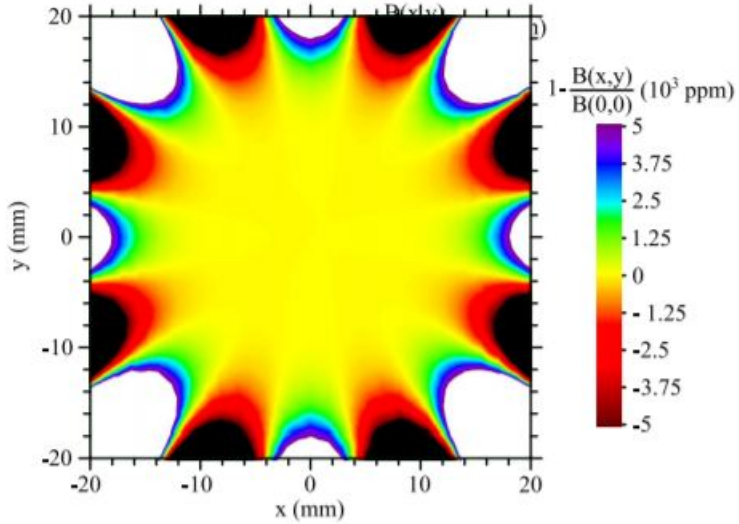

Figure 2.9: Simulation of the magnetic field B(x,y) along the x-y plane of the Halbach array magnet. Given values are realtive differences to the center value B(0,0).

surements by decreasing the size of the laser beam to less than 5 μm and a maximum optical magnification of 320 times.

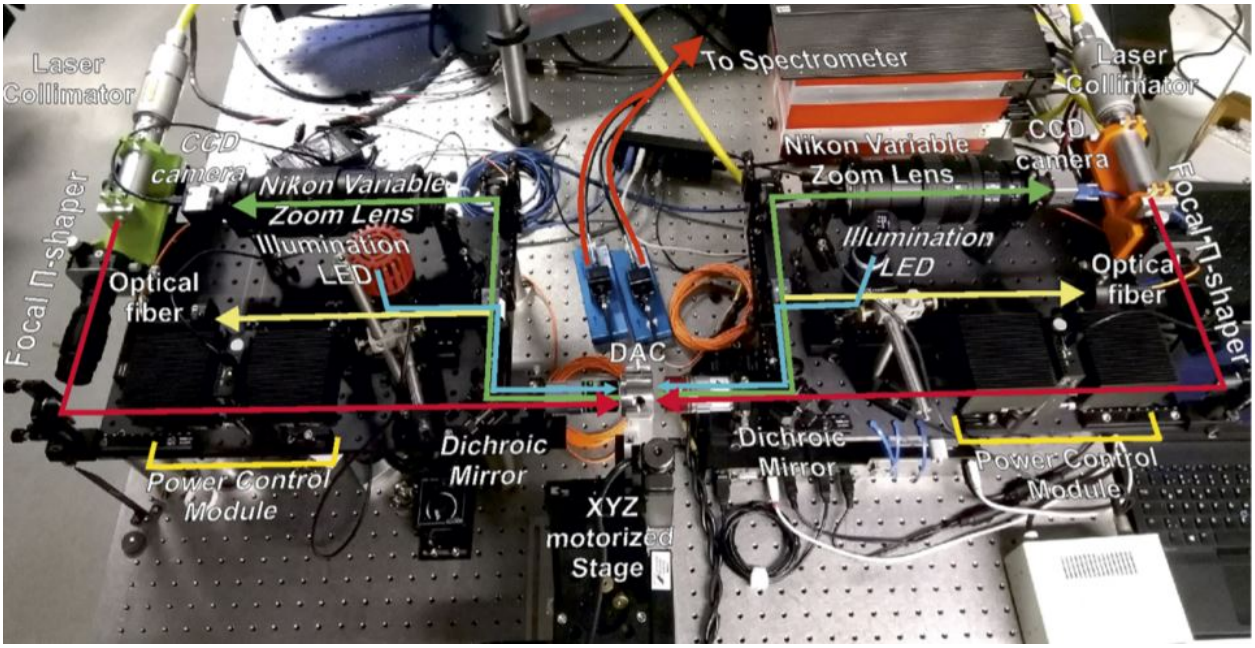

Figure 2.10: Laser heating configuration for in house experiments. Adapted from [37]

For our experiment, the Halbach array magnet with cell no. 2 positioned at its magnetic sweet spot was placed between the two objectives of the laser heating setup as shown in Figure 2.11. Laser heating operations were performed in continuous wave mode with a laser power of about 25 W. The preparation of anvils with focused ion beam milling for NMR measurements significantly reduces the quality of the anvil's surface in the pressure chamber, and renders them almost opaque. Hence the spectroradiometric temperature measurements with such anvils became possible only at relatively high temperatures (above 1500 K). For the temperature ranges achieved in this experiment (around 1100 K), the loss in the signal to noise ratio (SNR) in the time domain of the free induction decay are used.

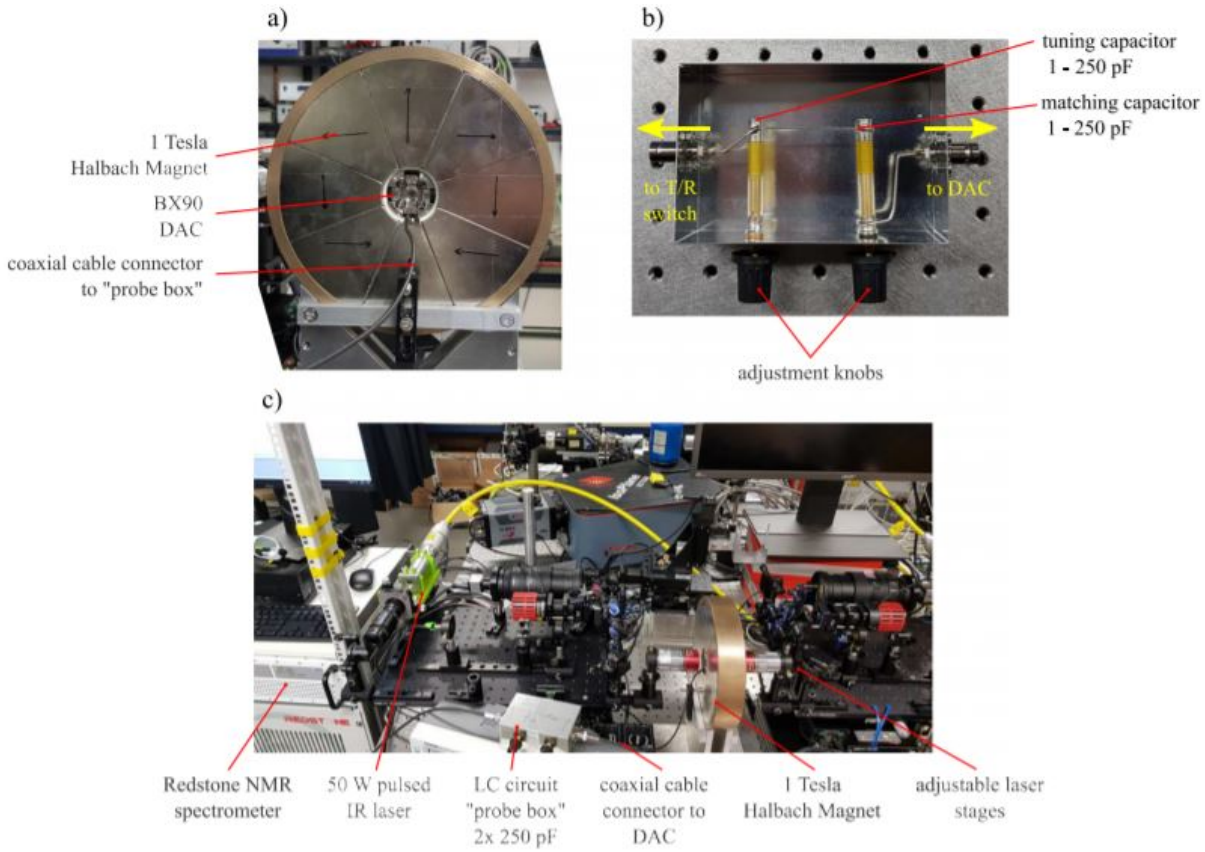

Figure 2.11: Table top high-pressure high-temperature NMR setup. (a) 1 T Halbach array magnet with a BX90 diamond anvil cell placed in its magnetic center.(b) NMR probe box with the tuning and matching capacitors. (c) Laser heating setup. [17]

2.2 Low-temperature NMR

NMR experiments to investigate Charge Density Wave order in Bi_2Se_3 were performed at the National High Magnetic Field Laboratory (Maglab) in Tallahassee, Florida. The external magnetic field is applied in two directions, one parallel to the c-axis of the crystal, and another perpendicular to the c-axis. The magnitude of the external magnetic field is 9.83 T and the NMR measurements were performed at temperatures ranging from 1.6 K to 300 K.

The Condensed Matter NMR group at Maglab utilizes a Janis ^{3}He refrigerator for low temperature NMR experiments, as described in the "^{3}He Refrigerator Installation and Operation" manual [38]. The system operates using a charcoal absorption (sorp) pump which

is in direct contact with ^{3}He gas within the cryostat. The ^{3}He gas, also in contact with the liquid-helium-cooled (L^{4}He) 1 K Pot, is first liquified by pumping on the pot below 3.2 K while keeping the sorp at high temperatures (>40 K). Thereafter, the charcoal is cooled down by circulating L^{4}He into the sorp. The large surface area of the charcoal cryo-pumps the gas resulting to lower ^{3}He vapor pressure. Through evaporative cooling, the low vapor pressure causes the liquid ^{3}He to cool below its boiling point, down to typically 0.3 K. A description of the ^{3}He cryostat is illustrated in Figure 2.18.

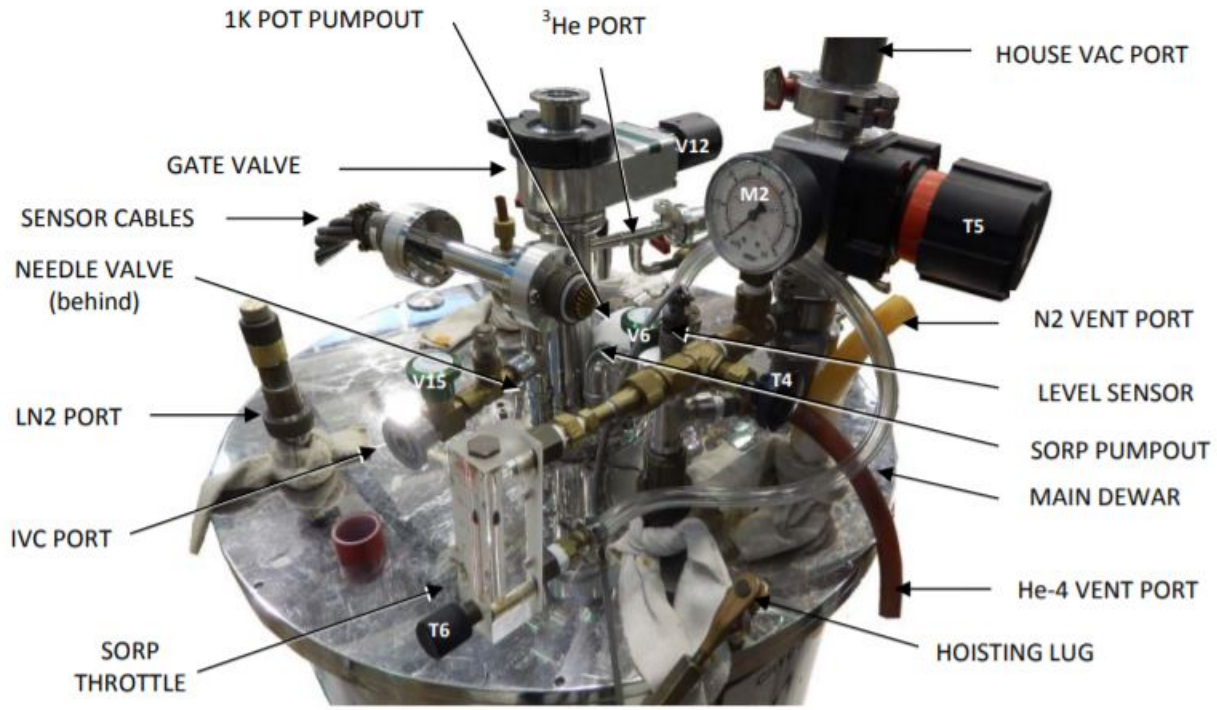

Figure 2.12: ^{3}He cryostat loaded into the dewar. Adapted from [38].

.

Pulsed ^{209}Bi NMR measurements are performed on a Bi_2Se_3 crystal of size ≈0.94 x 0.58 x 0.41 cm placed inside an 11 T Oxford Helium cryostat. The Bi_2Se_3 single crystal is studied with magnetic field oriented in two directions, parallel and perpendicular to the c-axis of the crystal. Spin-echo signals for ^{209}Bi NMR spectra are processed using the summed Fourier transform method, with field swept from 9.7 T to 10.5 T. Spin lattice relaxation time

(T_1) measurements in both parallel and perpendicular directions are performed at stabilized temperature points varying between 1.6 K and 300 K, with saturation pulses and typical time delays of 10 μs [39].

Chapter 3

High-Pressure High-Temperature NMR Results

3.1 Halbach array table-top high pressure NMR system

Figure 2.11 shows the experimental configuration. Figure 2.11 (a) shows the Halbach array magnet with the sample-loaded BX90 DAC mounted at its center. A 50 Ω coaxial cable connects the excitation coil of the DAC with the NMR probe box in Figure 2.11 (b). The probe box consists of two tunable high power capacitors with a 250 pF sweep range for frequency tuning and impedance matching. This probe box connects directly to a Redstone solid-state NMR spectrometer from *Tecmag Inc.*

Figure 3.1 shows the ^{1}H-NMR spectrum of Ice VII at 25 GPa at the highest field in the geometric center of the Halbach magnet. The signal's center of gravity was found at 43.1274 MHz corresponding to a B_0 field of 1013 mT. Table 3.1 shows the values of magnetic field and frequency at different positions of DAC in the Halbach array magnet. Values of magnetic field can be calculated from the values of frequency using Equation 1.1, with the

value of $\gamma = 2.675 * 10^8 s^{-1} T^{-1}$ as the gyromagnetic ratio of proton.

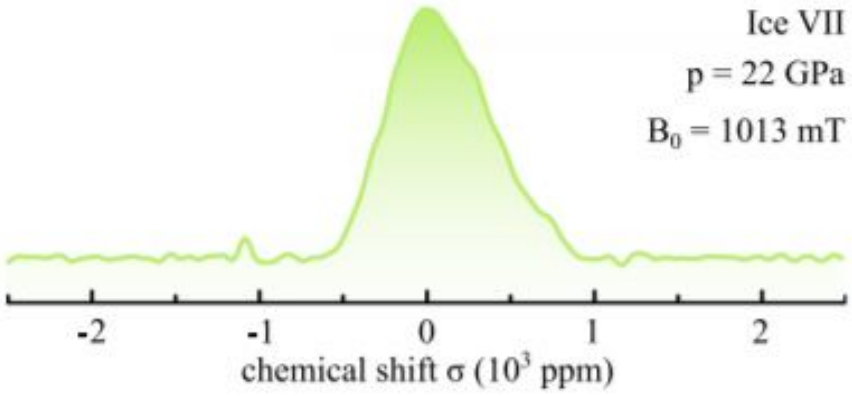

Figure 3.1: ^{1}H-NMR spectrum of Ice VII at 25 GPa and room temperature recorded in the magnetic sweet spot of the Halbach array magnet. [17]

Position from center (mm)	Magnetic field (mT)	Frequency (MHz)
0	1013	43.12740859
0.5	1013.2	43.13592338
1	1012.5	43.10612162
1.5	1012	43.08483464
2	1010.5	43.02097372
2.5	1010	42.99968675
3	1007.8	42.90602407
3.5	1005.2	42.7953318
-0.5	1013.1	43.13166599
-1	1012.7	43.11463641
-1.5	1011.5	43.06354767
-2	1010.5	43.02097372
-2.5	1009.8	42.99117196
-3	1007.7	42.90176667
-3.5	1003.9	42.73998567

Table 3.1: Magnetic field B_0 and frequency ω values measured at different positions of DAC in the Halbcah array magnet along the z-axis perpendicular to the place of the magnet.

The observed linewidth of about 43 kHz is similar to previous proton NMR resonances of ice VII at this magnetic field [3]. About 3000 scans are accumulated for each experiment.

Given an optimal relaxation delay of approximately $5.T_1$=0.35s, the total acquisition time per spectrum was about 18 minutes.

FEMM simulation of the Halbach magnet in Figure 1.3(b) and the numerical magnetic field simulation in Figure 2.9 show a fairly homogeneous B_0 field distribution in the x-y plane within a region of ±20 mm around its geometric center. However, as the diameter and length of the inner bore of the Halbach magnet are comparable in size, the B_0 field distribution can be expected to be very inhomogeneous along the z-direction. In fact, first test measurements using a roughly 3 mm long piece of rubber in a standard RF coil yielded a ^{1}H-NMR linewidths in the order of 20 kHz, which represents a 40-fold increase compared to standard electromagnet. However, given the microscopic dimensions of the sample chamber in the DAC, i.e., about 50 μm in diameter and 10 μm in thickness, this imhomogeneity is negligible and can be ignored.

As is evident from Figure 3.2 and Table 3.1. even with a relatively small region of ±4 mm off the center of the magnet, the magnetic field differs by 10 mT, corresponding to a 426 kHz in ^{1}H resonance frequencies. Moreover, at positions Δz> ±1 mm, a significant increase in the FWHM linewidth was observed. Using $\Delta\omega = \gamma_n \Delta B_0$, we find magnetic field gradients between 0.01 mT/μm at Δz=0 mm and 0.05 mT/μm at Δz=±4 mm. Fortunately, a magnetic "sweet spot" of about 1 mm near the geometric center was found, which exhibits average B_0 field values of 1013 mT and minimal magnetic field gradient of about 0.01 mT/μm over a sample cavity of 10 μm in height. This is shown in Figure 3.2. From this, we can assume magnetic field to be reasonably homogeneous at Δz=0 for samples smaller than 40 pl, which is the standard sample size for diamond anvil cell experiments in the megabar range.

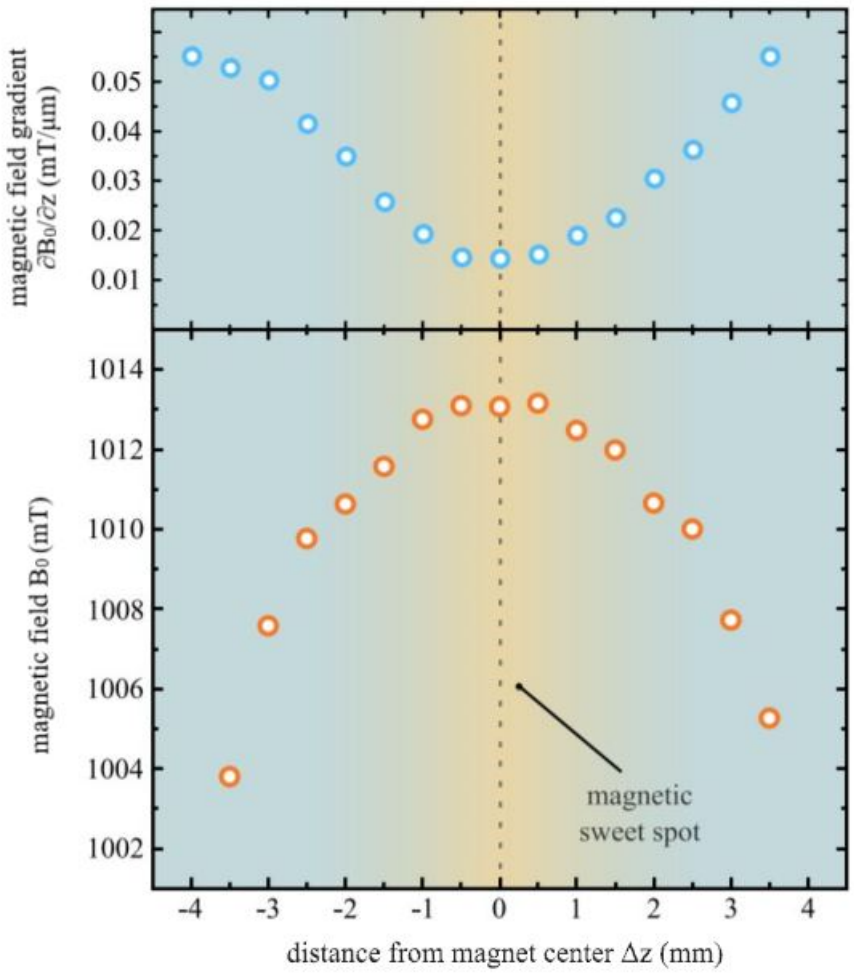

Figure 3.2: 1 mm wide magnetic sweet spot (golden region) with a homogeneous field of 1013 mT and 0.01 mT/μm field gradient. [17]. z-axis is perpendicular to the plane of the Halbach magnet.

3.2 *In situ* laser heating in NMR-DACs

Figure 2.11 (c) shows the table-top Halbach array setup combined with the double-sided laser heating system in Reference [37]. Laser experiments were conducted using a defocused laser spot of roughly 30 μm diameter, therefore we can assume for the whole sample cavity to have been heated. At room temperature, we found the signal to noise ratio (SNR) in the time domain of 0.534(5) per scan. Under continuous laser heating, the SNR decreased to 0.081(9), as can be observed in Figure 3.3. Using the scaling relationship [40, 41] $SNR \propto T^{-3/2}$, the

average temperature under laser heating T_{LH} within the sample cavity can be estimated to be

$$T_{LH} = 300K \left(\frac{SNR_{300}}{SNR_{LH}} \right)^{2/3} = 1063(50)K \tag{3.1}$$

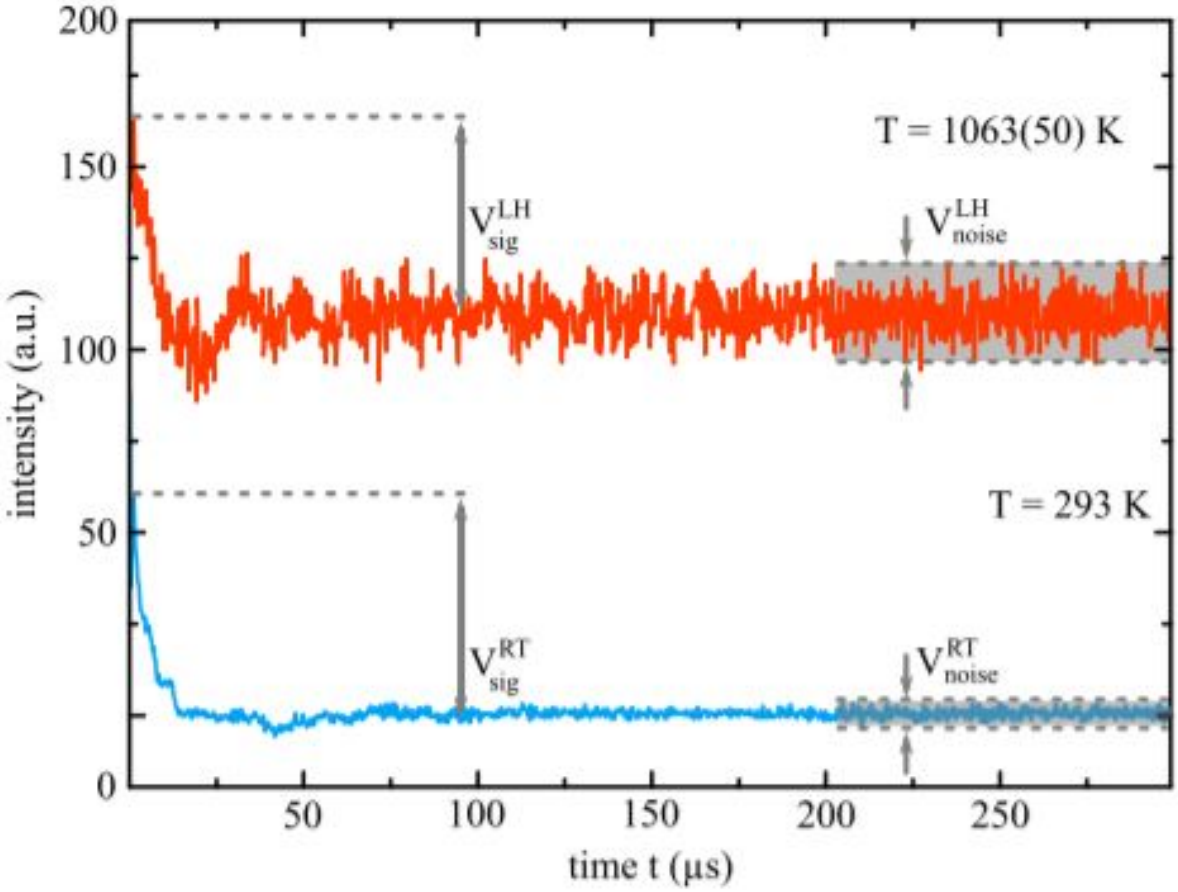

Figure 3.3: Comparison of signal voltage V_{sig} and noise voltage V_{noise} at ambient and high temperature under continuous wave laser heating conditions. [17]

.

Figure 3.4 shows a comparison of the measured ^{1}H-NMR spectra at ambient temperature and at elevated temperature under laser heating. At 1063 (50) K, a 100 ppm broad hydrogen resonance is observed at a chemical shift of σ=80 ppm.

After heating, the hydrogen resonances at room temperature were re-investigated and

found to be narrowed by approximately a factor of two. This effect likely originates from the thermal relaxation of stress distributions present before heating, and was caused by pressure gradients across the ice VII sample at 25 GPa.

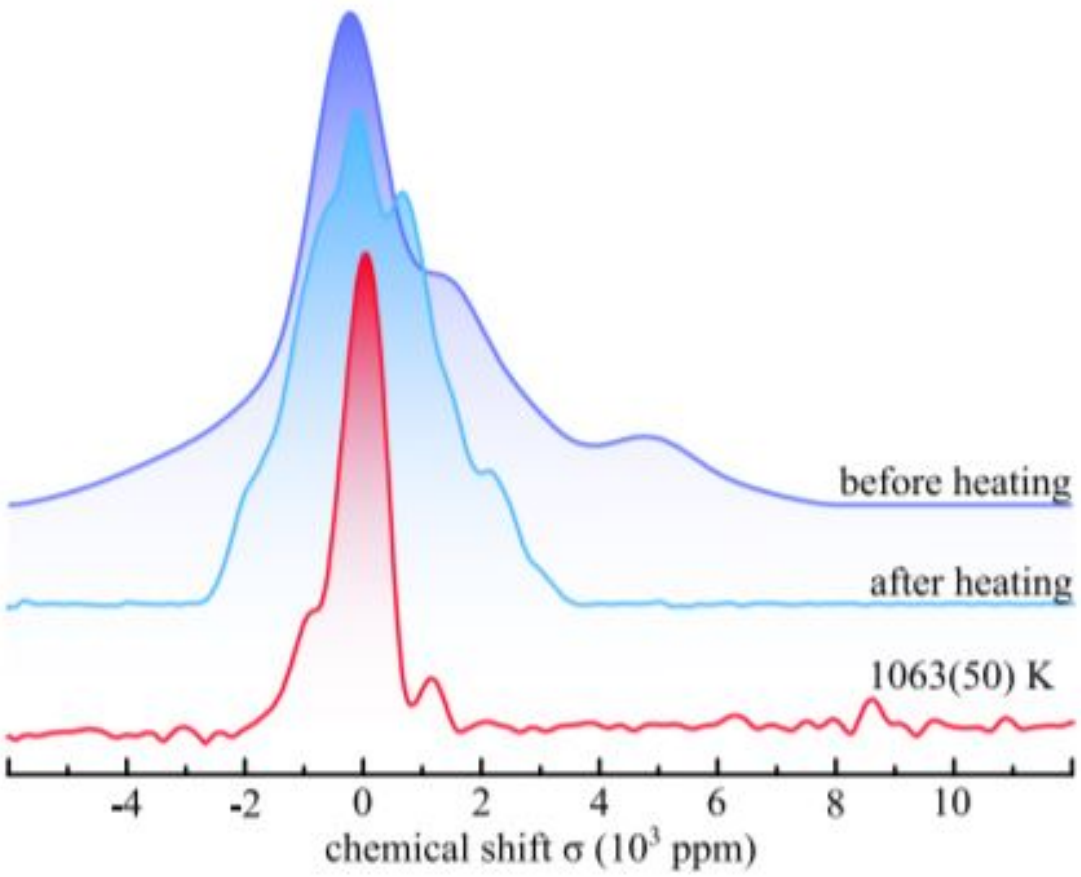

Figure 3.4: ^{1}H-NMR spectra of ice VII at 25 GPa at ambient temperature and 1063 K. [17]

.

3.3 Conclusion

This work develops a low-cost and space-saving NMR system which can be coupled with high-pressure and high-temperature instrumentation. Combining the Halbach array magnet with a regular spectrometer significantly reduces the space requirements of the whole setup. Furthermore, the permanent Halbach array magnet does not require maintenance,

in contrast to the high electrical costs of electromagnets or regular refill of cryogenic liquids in superconducting magnets. More importantly, this introduced setup yeilds ^{1}H-NMR signals of a similar spectral resolution in DAC-based experiments as standard electromagnets operating at the same magnetic fields of around 1 T [3]. The first application within a double sided laser heating system demonstrates the potential of this setup for simultaneous high-pressure and high-temperature NMR studies. Possible experiments include the investigation of electronic properties of superionic ices, which could have a significant impact on the field of geo- and planetary sciences. Moreover, the observation of formation of reaction products during laser heating assisted sample synthesis could be investigated, as well as melting and freezing dynamics. This setup can have wide applicability in high pressure solid state physics, chemistry, geosciences and even in biophysics communities, where the structure-function relationships of proteins under pressure can be studied [42].

Chapter 4

Low-temperature High-field NMR results

In this work led by my colleague Yanan Li [39] who is a PhD student in Dr. Guptasarma's lab, we report the experimental observations of Charge Density Wave (CDW) order in the topological insulator Bi_2Se_3, using resistivity measurements, electron diffraction and Nuclear Magnetic Resonance (NMR). In this thesis, we only report the NMR results. Detailed analysis of other results can be found in Reference [39] and in Appendix A2. Both resistivity and NMR results show a transition at around 140 K which together with electron diffraction results are a signature of CDW order.

Bi_2Se_3 is a topological insulator that exhibits strong spin-orbit coupling. The spin orbit coupling links the charge current to spin current via the spin Hall effect [43], described in section 1.5. Ideally, Bi_2Se_3 is a 3D topological insulator with a single Dirac cone [44]. In such materials, at energies near the Fermi level, the valence band and conduction band take the shape of upper and lower halves of a conical surface, meeting at what are called Dirac points, as shown in Figure 4.1. However, in 2010, Kuroda et al [45] reported the hexagonal deformation of the Fermi surface of Bi_2Se_3 using angle-resolved photoemission spectroscopy. A possible reason for such deviation from the ideal Dirac cone is the appearance of density

waves. Some studies have suggested towards the existence of CDW in Cu-Bi_2Se_3 [46, 47], but so far there has been no evidence of energy gap opening with temperature variation, indicating a CDW transition [39].

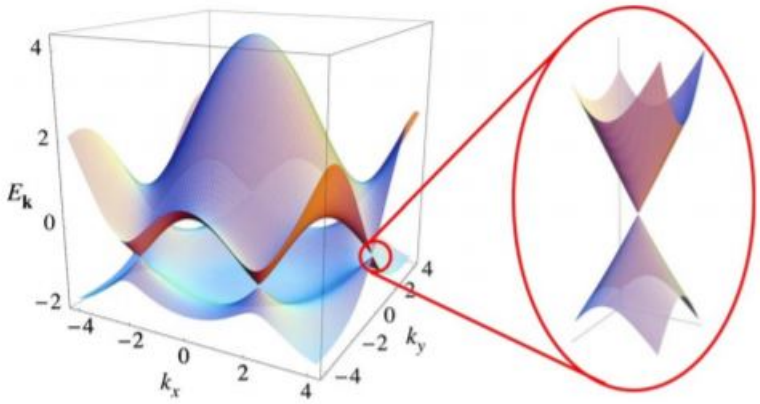

Figure 4.1: Zooming in on one of the Dirac points in graphene.Adapted from [48]

.

In Reference [39], we report the first direct observation of CDW order in Bi_2Se_3. The resistivity measurements shown in Figure A2 in Appendix A shows a metal-insulator-metal transition at around 140 K for different values of magnetic field. This transition is an indication of energy gap opening which is a characteristic of a CDW. Also shown in Figure A3 (Appendix A) are the images obtained from Transmission Electron Microscopy (TEM) and Selected Area Electron Diffraction (SAED) performed on a flake obtained from the Bi_2Se_3 single crystal. As seen in Figure A3(d), the diffraction pattern with the crystal tilted slightly off the <001> axis yields diffuse streaks between the diffraction spots, which is an indication of the Periodic Lattice Distortion associated with a CDW, also discussed in other previous studies [49, 50].

4.1 Magnetic field parallel to c-axis of crystal

When a magnetic field of 9.83 T is applied parallel to the c-axis of the crystal at different temperatures in the range of 1.6 - 300 K, the spin-lattice relaxation time (T_1) versus temperature graph as shown in Figure 4.1 is obtained. The red dashed line shows the fitting data. A transition is observed at 140 K, at which the slope of the curve changes from $T^{1.9}$ to $T^{5.9}$. Combined with other results described in the introductory section of this chapter and in Reference [39], we identify this as a transition to a CDW state below 140 K. Table 4.1 shows the NMR data used to plot Figure 4.2. The last column in Table 4.1 shows the fit values obtained using power-law fitting that yields the exponents $T^{1.9}$ and $T^{5.9}$. The uncertainty in these exponent values is ± 0.1. Another visible transition is observed at around 200 K where the exponent changes from $T^{5.9}$ to $T^{0.2}$.

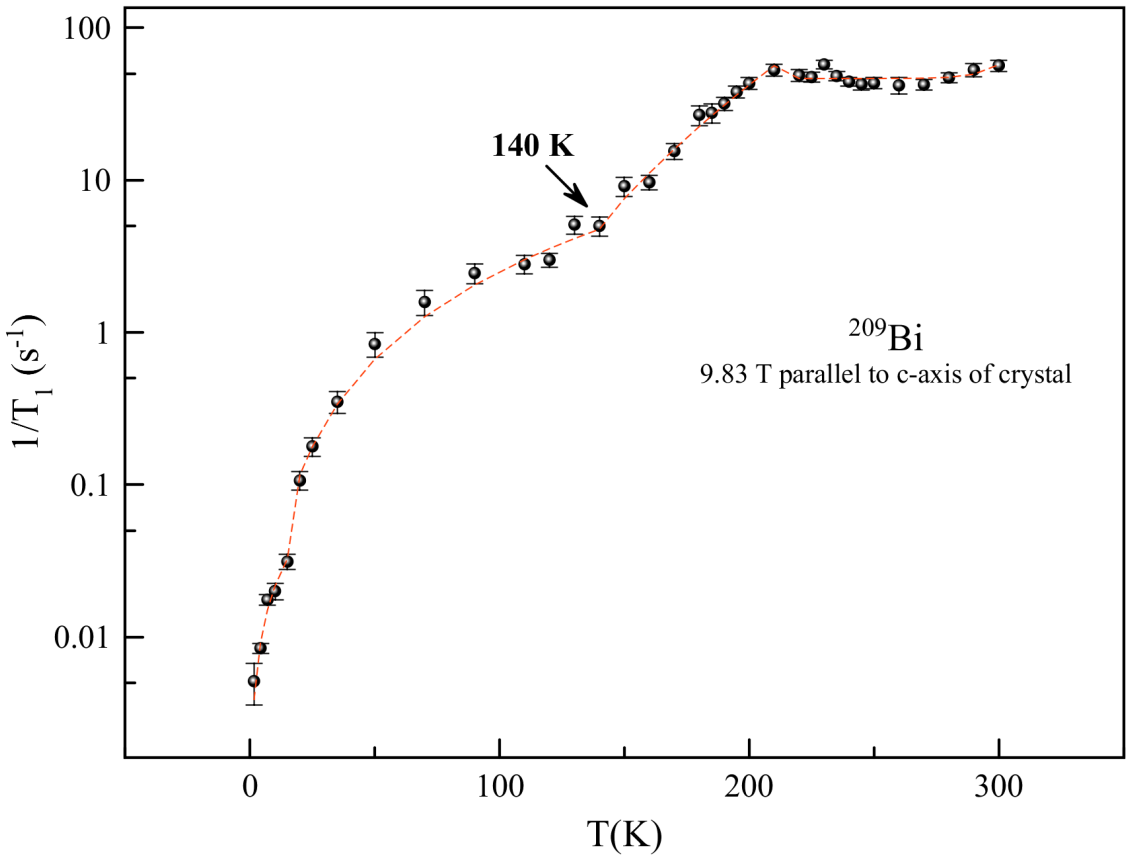

Figure 4.2: Spin-lattice relaxation rate $1/T_1$ as a function of temperature when magnetic field is applied parallel to the c-axis of the crystal. Temperature on the x-axis is plotted in a linear scale while the inverse of the spin-lattice relaxation time on the y-axis is plotted in logarithmic scale.

4.2 Magnetic field perpendicular to c-axis of crystal

When a magnetic field of 9.83 T is applied perpendicular to the c-axis of the crystal at different temperatures in the range of 1.7 - 300 K, the spin-lattice relaxation time (T_1) versus temperature graph as shown in Figure 4.2 is obtained. The red dashed line shows the fitting data. A transition is observed at 140 K, at which the slope of the curve changes from $T^{1.5}$ to $T^{8.1}$. Combined with other results described in the introductory section of this chapter and in Reference [39], we identify this as a transition to a CDW state below

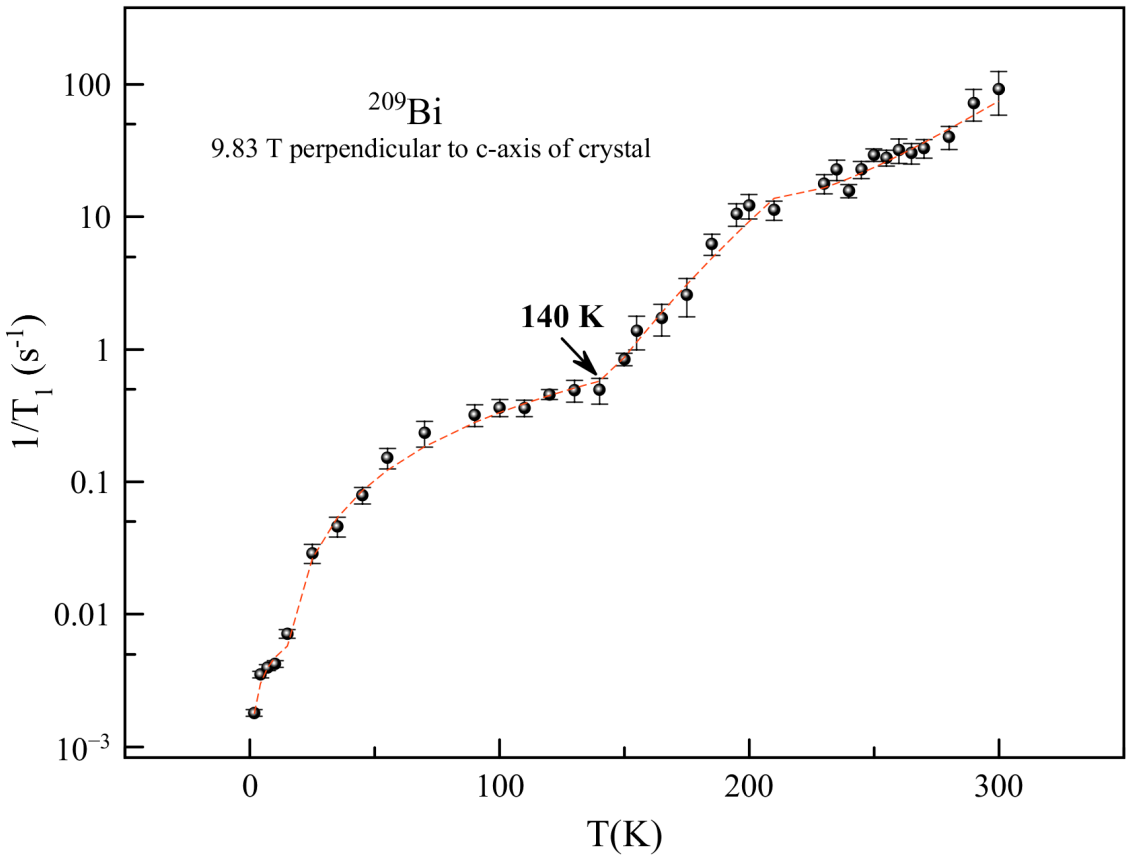

Figure 4.3: Spin-lattice relaxation rate $1/T_1$ as a function of temperature when magnetic field is applied perpendicular to the c-axis of the crystal. Temperature on the x-axis is plotted in a linear scale while the inverse of the spin-lattice relaxation time on the y-axis is plotted in logarithmic scale.

140K. Table 4.2 shows the NMR data used to plot Figure 4.3. The last column in Table 4.2 shows the fit values obtained using power-law fitting that yields the exponents $T^{1.5}$ and $T^{8.1}$. The uncertainty in these exponent values is ± 0.2. Another visible transition is observed at around 200 K where the exponent changes from $T^{8.1}$ to $T^{5.3}$.

In both cases where the magnetic field is applied in a direction parallel and perpendicular to the c-axis of the crystal, another transition around 200 K is also observed. The Debye temperature of Bi_2Se_3 is $\Theta_D \approx 182K$, and we attribute the near 200 K transition to the changes in the phonon spectrum across Θ_D.

The transition occurring near 15 K in Figure 4.2 agrees with the results of Young et al [51] when magnetic field is parallel to the c-axis. At low temperatures, we observe a linear Korringa-type relation, $1/T_{1,m}\alpha D^2(E_F)T$, where $D^2(E_F)$ is the density of states and $1/T_{1,m}$ includes the magnetic relaxation from conduction electron scattering. This implies that for the case of parallel field, the sample behaves like a metal at low temperature. In agreement with Young et al [51], this transition is likely due to a competition between magnetic and quadrupolar scattering. For the case of perpendicular field, the low temperature exponent is $T^{0.4}$, corresponding to magnetic relaxation in a semiconductor, for which $1/T_{1,m}\alpha NT^{1/2}$, where N is the charge carrier concentration. The difference in low temperature $1/T_1$ power laws for the parallel and perpendicular cases indicates the differences in conduction properties of Bi_2Se_3 along the quintuple layers and across the layers.

4.3 Conclusions

In the original work of Yanan Li [39] where I assisted with NMR measurements and data analysis, we present the evidence for the first experimental observation of Charge Density Wave (CDW) order in Bi_2Se_3. A metal to insulator transition at 140 K in resistivity measurements indicates the opening of a CDW-like energy gap. The diffused streaks in Selected Area Electron Diffraction indicate the presence of a periodic lattice distortion at room temperature which is also a characteristic of CDW. $1/T_1$ NMR measurements further support this 140 K transition both when the field is applied parallel and perpendicular to the c-axis of the crystal. NMR results also show two other transitions, one near 15 K and another near 200 K. Based on the temperature exponents along these transitions, we suggest that the 15 K transition results from a competition between magnetic and quadrupolar scattering. The 200 K scattering is not as clear - but we suggest that this could be a transition across the Debye temperature in Bi_2Se_3, or a transition to a first-order incommensurate CDW. Li et al [39] also discuss the impact of growth conditions that promote the formation of a

CDW: the strongly correlated ground states are present in Bi_2Se_3 crystals grown with high annealing and quenching temperature [39].

Appendices

Appendix A

Appendix 1

A.1 FEMM Simulation and Lua scripting

Version 4.2 of the Finite Element Method Magnetics (FEMM) was used to simulate the magnetic field intensity and density plot of the Halbach array magnet. Although FEMM is an excellent lightweight software with an easy to use interface for such purposes, there is not a direct way to export the values of the magnetic field intensity from each coordinate (point in space). Using the integrated Lua scripting language, we developed the script shown in Figure A.1 that outputs a file with a table of x and y coordinates and their corresponding magnetic field intensity values. This output file can then easily be used with any other data analysis program such as Origin, MATLAB, etc.

Lines 1 and 2 in the script denote the x-coordinates of the range of desired points, and line 3 denotes the length of increment in between this range. Lines 5-7 does the same for y-coordinates. Line 12 creates a new file with the input file name, and line 13 declares the variables (columns) that will be written in this new file. The *for* loop in lines 16-22 performs the extraction of the field values for all points in the x-y range.

```
x1=-45
x2=45
dx=0.001

y1=0
y2=0
dy=0.001

ni = (x2-x1)/dx+2
nj = (y2-y1)/dy+2

handle=openfile("B2.dat","w")
write(handle,"VARIABLES = x y B Bx Byn")
write(handle,format("ZONE I=%d J=%dn",ni,nj))

for j=0,nj-1,1 do
  for i=0,ni-1,1 do
  x=x1+i*dx
  y=y1+j*dy
  A,B1,B2=mo_getpointvalues(x,y)
  write(handle,x," ",y," ",sqrt(B1*B1+B2*B2)," ",B1," ",B2,"n")
 end
end

closefile(handle)
```

Figure A.1: Lua script to extract magnetic field intensity values from FEMM into a text file.

.

A.2 Charge Density Wave order in Bi_2Se_3

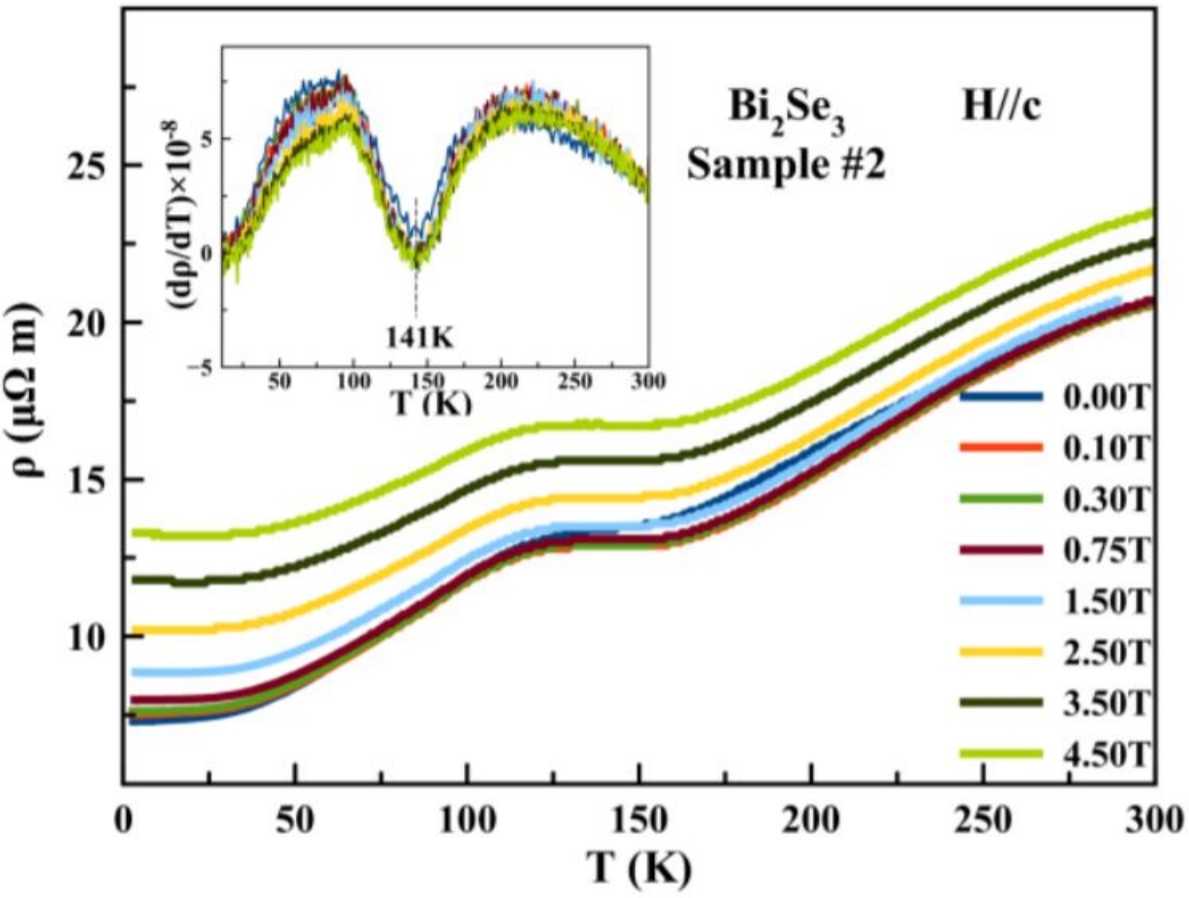

Figure A.2: Thermal dependence of resistivity of Bi_2Se_3 for different values of applied magnetic field varying between 0.00 - 4.50 T, applied paralled to the c-axis of the crystal. [39]

.

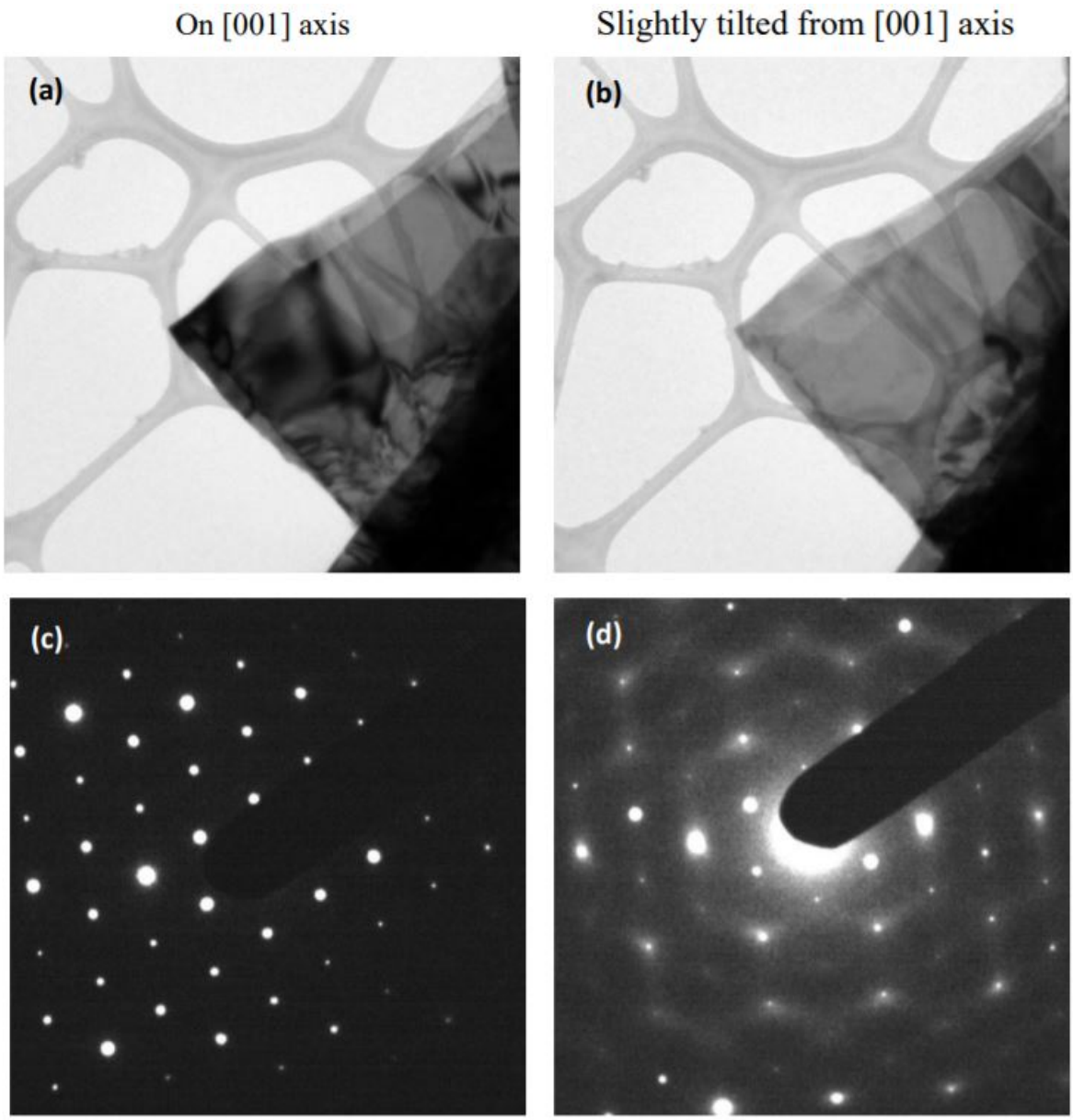

Figure A.3: **a,b** Bright field Transmission Electron Microscopy on a flake obtained from single crystal of Bi_2Se_3. **c,d** Selected Area Electron Diffraction from the corresponding areas shown in (a) and (b) respectively. (a) and (c) are images when the electron beam is on <001> axis. (b) and (d) are images of off-axis electron diffraction, for which the sample was tilted slightly (less than 5 degrees) away from the zone axis. [39]

.

T(K)	1/T1 (1/s)	Error	Fit
1.6	0.005129257	0.001565402	0.00385107
4.2	0.008448372	6.44E-04	0.009132673
7	0.0175679	0.001355508	0.015059596
10	0.020015692	0.002463261	0.021573949
15	0.03125	0.003552637	0.032686131
20	0.106503078	0.014745777	0.116118289
25	0.178504489	0.025207494	0.17774412
35	0.350017501	0.056674167	0.337748106
50	0.838222967	0.151400071	0.667006969
70	1.583130165	0.292485341	1.267441873
90	2.449179525	0.365787331	2.047221266
110	2.801120448	0.38839065	3.002192976
120	2.991325157	0.322128943	3.544340194
130	5.104905814	0.690591679	4.129124924
140	5	0.715	4.756233634
150	9.124087591	1.297934759	7.55689611
160	9.661835749	1.053560176	11.10842555
170	15.49666822	1.807824552	15.95200252
180	26.80246583	3.986965568	22.43841343
185	27.64141347	3.911924422	26.42536467
190	31.81876034	3.180559871	30.98528556
195	37.93195008	3.314207557	36.18212838
200	43.17789292	3.971023831	42.08504135
210	52.79831045	4.488135155	56.31329277
220	48.75694177	4.169677856	46.39592739
225	47.39538653	3.398686192	46.39608975
230	57.40528129	3.479906833	46.39644724
235	48.21600771	3.301192428	46.39722104
240	44.24778761	2.799749393	46.39886872
245	42.62574595	3.50672164	46.40232249
250	43.30879168	3.721292451	46.40945381
260	41.84800803	5.280036166	46.45309551
270	42.33700254	3.220981946	46.62355982
280	47.08097928	3.664070563	47.2568611
290	52.91005291	5.263010554	49.50265831
300	56.55852676	4.830289094	57.12862731

Table A.1: NMR data showing temperature and $1/T_1$ with corresponding error values when field is applied parallel to the c-axis. Last column shows the values of $1/T_1$ obtained from power-law fitting.

T(K)	1/T1 (1/s)	Error	Fit
1.7	0.00179839	0.000101137	0.001773241
4.2	0.003520619	0.000213958	0.003003661
7	0.003965626	0.000203324	0.003938044
10	0.00422581	0.000259576	0.004721504
15	0.007129108	0.000496725	0.005768727
25	0.02887703	0.004813172	0.026464224
35	0.046111424	0.007954989	0.053679535
45	0.079365079	0.011557067	0.085829601
55	0.152237125	0.02688896	0.122409899
70	0.234886796	0.051690466	0.184815842
90	0.320463518	0.060538776	0.280768428
100	0.362871036	0.053951357	0.333778139
110	0.36125993	0.05175846	0.389943139
120	0.45627307	0.038489264	0.449138628
130	0.492467706	0.09183188	0.511255028
140	0.49638138	0.108980276	0.576195064
150	0.84234644	0.088877923	0.870989238
155	1.383968113	0.388915419	1.140319306
165	1.728229066	0.465907142	1.906059628
175	2.586057529	0.828203969	3.091110705
185	6.261740764	1.125466543	4.880013297
195	10.56589898	2.035388051	7.521168434
200	12.231204	2.556853787	9.260498963
210	11.34058148	1.860454731	13.82760159
230	17.86231017	2.980327399	16.59604652
235	22.85891932	4.06220197	17.96978091
240	15.75659216	1.882285323	19.58004806
245	22.9084578	3.4465547	21.46134034
250	29.46271788	3.234360801	23.65231019
255	27.98032424	3.755251158	26.19617138
260	32.06464232	6.746046241	29.14112979
265	30.46866907	5.300820228	32.54084495
270	33.14056571	5.391430612	36.45492422
280	40.25975595	7.908441312	46.09754826
290	72.4837274	19.32591169	58.68579347
300	92.42571283	33.4319765	74.96928308

Table A.2: NMR data showing temperature and $1/T_1$ with corresponding error values when field is applied perpendicular to the c-axis. Last column shows the values of $1/T_1$ obtained from power-law fitting.

Bibliography

[1] C. G. Pruteanu, G. J. Ackland, W. C. Poon, and J. S. Loveday, "When immiscible becomes miscible—methane in water at high pressures," *Science Advances*, vol. 3, no. 8, p. e1700240, 2017.

[2] X. Dong, A. R. Oganov, A. F. Goncharov, E. Stavrou, S. Lobanov, G. Saleh, G.-R. Qian, Q. Zhu, C. Gatti, V. L. Deringer, *et al.*, "A stable compound of helium and sodium at high pressure," *Nature Chemistry*, vol. 9, no. 5, pp. 440–445, 2017.

[3] T. Meier, S. Petitgirard, S. Khandarkhaeva, and L. Dubrovinsky, "Observation of nuclear quantum effects and hydrogen bond symmetrisation in high pressure ice," *Nature Communications*, vol. 9, no. 1, pp. 1–7, 2018.

[4] T. Meier, F. Trybel, S. Khandarkhaeva, G. Steinle-Neumann, S. Chariton, T. Fedotenko, S. Petitgirard, M. Hanfland, K. Glazyrin, N. Dubrovinskaia, *et al.*, "Pressure-induced hydrogen-hydrogen interaction in metallic FeH revealed by NMR," *Physical Review X*, vol. 9, no. 3, p. 031008, 2019.

[5] Y. Sun, J. Lv, Y. Xie, H. Liu, and Y. Ma, "Route to a superconducting phase above room temperature in electron-doped hydride compounds under high pressure," *Physical Review Letters*, vol. 123, no. 9, p. 097001, 2019.

[6] J. C. Slater, "P. W. Bridgman and high-pressure physics," *Science*, vol. 148, no. 3671, pp. 805–86, 1965.

[7] N. Dubrovinskaia, L. Dubrovinsky, N. A. Solopova, A. Abakumov, S. Turner, M. Hanfland, E. Bykova, M. Bykov, C. Prescher, V. B. Prakapenka, *et al.*, "Terapascal static pressure generation with ultrahigh yield strength nanodiamond," *Science Advances*, vol. 2, no. 7, p. e1600341, 2016.

[8] P. C. Burnley, "The Diamond Anvil Cell," *University of Nevada, Las Vegas*.

[9] J.-F. Lin, J. Shu, H.-k. Mao, R. J. Hemley, and G. Shen, "Amorphous boron gasket in diamond anvil cell research," *Review of Scientific Instruments*, vol. 74, no. 11, pp. 4732–4736, 2003.

[10] N. Funamori and T. Sato, "A cubic boron nitride gasket for diamond-anvil experiments," *Review of Scientific Instruments*, vol. 79, no. 5, p. 053903, 2008.

[11] G. Zou, Y. Ma, H.-k. Mao, R. J. Hemley, and S. A. Gramsch, "A diamond gasket for the laser-heated diamond anvil cell," *Review of Scientific Instruments*, vol. 72, no. 2, pp. 1298–1301, 2001.

[12] A. Spyros and P. Dais, "31p NMR spectroscopy in food analysis," *Progress in Nuclear Magnetic Resonance Spectroscopy*, vol. 54, no. 3-4, pp. 195–207, 2009.

[13] N. Spengler, P. T. While, M. V. Meissner, U. Wallrabe, and J. G. Korvink, "Magnetic lenz lenses improve the limit-of-detection in nuclear magnetic resonance," *PloS One*, vol. 12, no. 8, 2017.

[14] J. Schoenmaker, K. Pirota, and J. Teixeira, "Magnetic flux amplification by lenz lenses," *Review of Scientific Instruments*, vol. 84, no. 8, p. 085120, 2013.

[15] T. Meier, N. Wang, D. Mager, J. G. Korvink, S. Petitgirard, and L. Dubrovinsky, "Magnetic flux tailoring through lenz lenses for ultrasmall samples: A new pathway to high-pressure nuclear magnetic resonance," *Science Advances*, vol. 3, no. 12, p. eaao5242, 2017.

[16] T. Meier, S. Khandarkhaeva, S. Petitgirard, T. Körber, A. Lauerer, E. Rössler, and L. Dubrovinsky, "NMR at pressures up to 90 GPa," *Journal of Magnetic Resonance*, vol. 292, pp. 44–47, 2018.

[17] T. Meier, A. P. Dwivedi, S. Khandarkhaeva, T. Fedotenko, N. Dubrovinskaia, and L. Dubrovinsky, "Table-top nuclear magnetic resonance system for high-pressure studies with in situ laser heating," *Review of Scientific Instruments*, vol. 90, no. 12, p. 123901, 2019.

[18] C. L. Kane and E. J. Mele, "Quantum spin Hall effect in graphene," *Physical Review Letters*, vol. 95, no. 22, p. 226801, 2005.

[19] B. A. Bernevig and S.-C. Zhang, "Quantum spin Hall effect," *Physical Review Letters*, vol. 96, no. 10, p. 106802, 2006.

[20] C. L. Kane and E. J. Mele, "Z 2 topological order and the quantum spin Hall effect," *Physical Review Letters*, vol. 95, no. 14, p. 146802, 2005.

[21] X.-L. Qi and S.-C. Zhang, "The quantum spin Hall effect and topological insulators," *Physics Today*, vol. 63, no. 1, p. 33, 2010.

[22] N. H. Lindner, G. Refael, and V. Galitski, "Floquet topological insulator in semiconductor quantum wells," *Nature Physics*, vol. 7, no. 6, pp. 490–495, 2011.

[23] N. P. Ong, "Sliding charge density wave," *Princeton University*, p. http://www.physics.princeton.edu/ npo/SurveyTopics/ChargeDensityWave.html, Retrieved June 2, 2020.

[24] H. Bhadeshia, "Phase changes and charge density waves," *Physical Metallurgy*, vol. 5, 2014.

[25] K. Cho, M. Kończykowski, S. Teknowijoyo, M. A. Tanatar, J. Guss, P. Gartin, J. M. Wilde, A. Kreyssig, R. McQueeney, A. I. Goldman, *et al.*, "Using controlled disorder

to probe the interplay between charge order and superconductivity in $NbSe_2$," *Nature Communications*, vol. 9, no. 1, pp. 1–9, 2018.

[26] S. J. Denholme, A. Yukawa, K. Tsumura, M. Nagao, R. Tamura, S. Watauchi, I. Tanaka, H. Takayanagi, and N. Miyakawa, "Coexistence of superconductivity and charge-density wave in the quasi-one-dimensional material $HfTe_3$," *Scientific Reports*, vol. 7, p. 45217, 2017.

[27] S. Yasuzuka, K. Murata, T. Fujimoto, M. Shimotori, and K. Yamaya, "Coexistence of the upper charge-density-wave and the superconductivity in $NbSe_3$," *Journal of the Physical Society of Japan*, vol. 74, no. 6, pp. 1782–1786, 2005.

[28] L. Fang, P. Zou, Y. Wang, L. Tang, Z. Xu, H. Chen, C. Dong, L. Shan, and H. Wen, "Competition of superconductivity and charge density wave order in Na_xTaS_2 single crystals," *Science and Technology of Advanced Materials*, vol. 6, no. 7, pp. 736–739, 2005.

[29] D. Bhoi, S. Khim, W. Nam, B. Lee, C. Kim, B.-G. Jeon, B. Min, S. Park, and K. H. Kim, "Interplay of charge density wave and multiband superconductivity in 2H-Pd_xTaSe_2," *Scientific Reports*, vol. 6, no. 1, pp. 1–10, 2016.

[30] I. Kantor, V. Prakapenka, A. Kantor, P. Dera, A. Kurnosov, S. Sinogeikin, N. Dubrovinskaia, and L. Dubrovinsky, "BX90: A new Diamond Anvil Cell design for X-ray diffraction and optical measurements," *Review of Scientific Instruments*, vol. 83, no. 12, p. 125102, 2012.

[31] E. L. Hahn, "Spin echoes," *Physical Review*, vol. 80, no. 4, p. 580, 1950.

[32] G. B. Chavhan, P. S. Babyn, B. Thomas, M. M. Shroff, and E. M. Haacke, "Principles, techniques, and applications of T2*-based MR imaging and its special applications," *Radiographics*, vol. 29, no. 5, pp. 1433–1449, 2009.

[33] "Free induction decay," *Wikipedia*, p. https://en.wikipedia.org/wiki/Free induction decay, Retrieved May 26, 2020.

[34] "T2* vs T2 relaxation time," *Questions and Answers in MRI*, pp. http://mriquestions.com/t2–vs–t2.html, Retrieved May 26, 2020.

[35] "Spin echo," *Questions and Answers in MRI*, pp. http://mriquestions.com/spin–echo1.html, Retrieved May 26, 2020.

[36] "Ice VI," *Wikipedia*, p. https://en.wikipedia.org/wiki/Ice VI, Retrieved May 26, 2020.

[37] T. Fedotenko, L. Dubrovinsky, G. Aprilis, E. Koemets, A. Snigirev, I. Snigireva, A. Barannikov, P. Ershov, F. Cova, M. Hanfland, *et al.*, "Laser heating setup for Diamond Anvil Cells for *in situ* synchrotron and *in house* high and ultra-high pressure studies," *Review of Scientific Instruments*, vol. 90, no. 10, p. 104501, 2019.

[38] "^{3}He refrigerator installation and operation, Condensed Matter NMR," pp. https://nationalmaglab.org/images/users/dc–field/searchable–docs/sample–environments/nmr3he/manual.pdf, Retrieved June 2, 2020.

[39] Y. Li, C. Parsons, S. Ramakrishna, A. Dwivedi, M. Schofield, A. Reyes, and P. Guptasarma, "Charge Density Wave order in the topological insulator Bi_2Se_3," *arxiv:2002.12546*.

[40] E. Fukushima and S. Roeder, "Experimental pulse NMR: A nuts and bolts approach," vol. 1st ed., 1994.

[41] M. L. J. Mispelter and A. Briguet, "NMR probeheads for Biophysical and Biomedical experiments," vol. 2nd ed., 1994.

[42] M. Gross and R. Jaenicke, "Proteins under pressure: the influence of high hydrostatic pressure on structure, function and assembly of proteins and protein complexes," *European Journal of Biochemistry*, vol. 221, no. 2, pp. 617–630, 1994.

[43] P. Deorani, J. Son, K. Banerjee, N. Koirala, M. Brahlek, S. Oh, and H. Yang, "Observation of inverse spin hall effect in bismuth selenide," *Physical Review B*, vol. 90, no. 9, p. 094403, 2014.

[44] Y. Xia, D. Qian, D. Hsieh, L. Wray, A. Pal, H. Lin, A. Bansil, D. Grauer, Y. S. Hor, R. J. Cava, *et al.*, "Observation of a large-gap topological-insulator class with a single Dirac cone on the surface," *Nature Physics*, vol. 5, no. 6, pp. 398–402, 2009.

[45] K. Kuroda, M. Arita, K. Miyamoto, M. Ye, J. Jiang, A. Kimura, E. Krasovskii, E. Chulkov, H. Iwasawa, T. Okuda, *et al.*, "Hexagonally deformed fermi surface of the 3d topological insulator Bi_2Se_3," *Physical Review Letters*, vol. 105, no. 7, p. 076802, 2010.

[46] K. J. Koski, C. D. Wessells, B. W. Reed, J. J. Cha, D. Kong, and Y. Cui, "Chemical intercalation of zerovalent metals into 2d layered Bi_2Se_3 nanoribbons," *Journal of the American Chemical Society*, vol. 134, no. 33, pp. 13773–13779, 2012.

[47] M. Wang and K. J. Koski, "Polytypic phase transitions in metal intercalated Bi_2Se_3," *Journal of Physics: Condensed Matter*, vol. 28, no. 49, p. 494002, 2016.

[48] A. C. Neto, F. Guinea, N. M. Peres, K. S. Novoselov, and A. K. Geim, "The electronic properties of graphene," *Reviews of Modern Physics*, vol. 81, no. 1, p. 109, 2009.

[49] C. Swenson, R. Shelton, P. Klavins, and H. Yang, "Thermal-expansion measurements for $Lu_5Ir_4Si_{10}$, $Lu_5Rh_4Si_{10}$, $Sc_5Ir_4Si_{10}$, and $Tm\,5\,Ir_4Si_{10}$: Charge-density-wave effects," *Physical Review B*, vol. 43, no. 10, p. 7668, 1991.

[50] A. Zong, X. Shen, A. Kogar, L. Ye, C. Marks, D. Chowdhury, T. Rohwer, B. Freelon, S. Weathersby, R. Li, *et al.*, "Ultrafast manipulation of mirror domain walls in a charge density wave," *Science Advances*, vol. 4, no. 10, p. eaau5501, 2018.

[51] B.-L. Young, Z.-Y. Lai, Z. Xu, A. Yang, G. Gu, Z.-H. Pan, T. Valla, G. Shu, R. Sankar, and F. Chou, "Probing the bulk electronic states of Bi_2Se_3 using nuclear magnetic resonance," *Physical Review B*, vol. 86, no. 7, p. 075137, 2012.